Twinning mediated intralayer frustration governs structural degradation in layered Li-rich oxide cathode

Tingting Yang[1, 2, #], Maolin Yang[1, #], Zhongyuan Huang[1], Rui Wang[3], Wenhai Ji[4], Peng-Han Lu[2], Tao Zeng[1], Zenan Li[5], Jun Wang[5], Rafal E. Dunin-Borkowski[2], Lei Jin[2*], Yinguo Xiao[1*]

[1]School of Advanced Materials, Peking University, Shenzhen Graduate School, Shenzhen 518055, PR China

[2]Ernst Ruska-Centre for Microscopy and Spectroscopy with Electrons, Forschungszentrum Jülich GmbH, 52425 Jülich, Germany

[3]Department of Engineering, University of Cambridge, Cambridge CB30FS, UK

[4]Spallation Neutron Source Science Center, Dongguan 523803, PR China

[5]School of Innovation and Entrepreneurship, Southern University of Science and Technology, Shenzhen 518055, PR China

[#]These authors (T. Yang and M. Yang) contributed equally to this work.

[*]E-mail addresses: l.jin@fz-juelich.de (L. Jin); y.xiao@pku.edu.cn (Y. Xiao).

Abstract

Layered Li-rich Mn-based (LRM) oxides are promising cathode materials for next-generation high-energy batteries. However, their commercialization is hindered by intrinsic structural issues and subsequent degradation processes. In order to address the degradation mechanisms, we use *operando* neutron diffraction and scanning transmission electron microscopy to follow the microstructural degeneration of the LRM oxides in a prepared full cell with a graphite anode. The methods enable both real-time phase analysis and structural evolution mapping across a wide field of view. The LRM oxide is observed to initially have a partially-ordered Li_2MnO_3-like structure with multiple planar defects. It transitions from an ordered monoclinic phase to a disordered rhombohedral phase as a result of irreversible Li ion migration and transition metal rearrangement during cycling. Especially after first fully charged, the interlayer (001) twining-like structures and local intralayer frustrations formed. Over cycling, the intralayer frustrations further develop into pore-like microstructures along the {012} twinning boundary in the bulk of the particles, which contributes significantly to performance reduction. The results clarify the link between microstructure degradation and performance loss and provide valuable insights into the optimization of high-performance cathodes.

Introduction

The stability of the primary framework structure of an intercalation compound profoundly influences the reversibility of its structural evolution during ion insertion and extraction.[1-4] Practical applications of layered cathode materials for Li-ion batteries, such as Li-rich Mn-based (LRM) cathodes, require heightened stability of their transition metal (TM) layer framework due to the exceptional number of intercalated ions that they can accommodate.[5-7] Although LRM cathode materials have an impressive energy density of ~900 Wh kg^{-1} due to their high working voltage and substantial ion intercalation and deintercalation capacity,[8,9] anion oxidation,[10,11] oxygen release,[12,13] irreversible damage from ion intercalation[5,14,15] and complex interface reactions induced by a high cutoff voltage[16,17] pose severe challenges for practical

applications of LRM cathodes. Despite numerous studies on surface modification strategies to mitigate oxygen release, voltage decay remains a significant issue.[18-20]

Studies of the failure mechanisms of LRM cathodes must focus on both interface structure and bulk structure. By employing high-precision resonant inelastic X-ray scattering and ^{17}O solid-state nuclear magnetic resonance techniques, House *et al.* found that O_2 can form in a typical $Li_{1.2}Ni_{0.13}Co_{0.13}Mn_{0.54}O_2$ cathode and stay in the lattice during charging.[21] Density functional theory calculations showed that TM layer rearrangement during Li deintercalation creates vacancy clusters and alters the charge compensation mechanism during discharge, contributing to voltage decay. Similar O vacancy migration behavior has been observed in $Li_{1.18}Mn_{0.53}Ni_{0.21}Co_{0.08}O_2$ layered cathodes using scanning transmission soft X-ray microscopy and X-ray electron layer diffraction imaging.[22] However, these studies focused on O electronic structure and did not track TM movement. Unfortunately, current research often relies on assumptions and inferences obtained from LRM cathode microstructures examined under specific conditions that do not reflect operational environments.[23-25] The lack of systematic research on failure structures in LRM cathodes means that the structural evolution of LRM cathodes over their full lifecycles remains elusive.

In order to elucidate the true structural evolution of LRM cathode materials, the present study combines *operando* neutron diffraction, which has high sensitivity to both light elements and adjoining TMs, with four-dimensional scanning transmission electron microscopy (4D-STEM), phase analysis and atomic-resolution aberration-corrected electron microscopy, which provide complementary information about long and short-range structure. Such a multiscale approach reveals the initial lattice structure, TM rearrangement, phase and structure evolution, defect growth and structural failure.

Results

Structure of the pristine LRM cathode

The failure mechanism of a representative LRM cathode material of nominal

composition $Li_{1.2}Ni_{0.13}Co_{0.13}Mn_{0.54}O_2$ was studied during an electrochemical process. A protective spinel layer was introduced onto the surface of the LRM oxide during synthesis, as shown in Supplementary Fig. 1a, b, to ensure consistent electrochemical performance in a pouch cell. The morphology of the untreated LRM oxide (u-LRM) was shown in Supplementary Fig. 1c, d. Supplementary Fig. 2 shows that the electrochemical performance u-LRM cathode and synthesized LRM, which indicate that u-LRM exhibits a significantly lower initial Coulombic efficiency (ICE) compared to the surface-reconstructed sample (85% vs. 91%), suggesting a higher extent of irreversible oxygen redox reactions in the u-LRM. The results also show distinctive electrochemical characteristics in half-cell assessments, such as a characteristic O redox plateau during the initial charge cycle, voltage hysteresis during discharge and subsequent cycle-induced voltage decay.[26]

Neutron powder diffraction (NPD) and Rietveld refinement reveal that the pristine LRM oxide comprises 97.27% of an O3' phase (space group: $C2/m$), and 2.73% of a spinel phase (denoted S, space group: $Fd\bar{3}m$) (Fig. 1a). Comprehensive structural information is provided in Supplementary Table 1. Additionally, the residual negative scattering signal observed at the tetrahedral sites in the Fourier difference map (Supplementary Fig. 3) of the O3' phase from the neutron diffraction pattern indicates Li^+ occupation at tetrahedral sites, aligning with spinel structure features and corroborating the existence of spinel phase in LRM. 4D-STEM analysis was performed to determine the phase distribution in an entire LRM particle. The technique involves recording convergent beam electron diffraction patterns in a two-dimensional grid of electron probe positions. Data processing can be used to provide information about material properties, including phase, orientation, strain and electromagnetic field distribution.[27] The representative 4D-STEM results in Fig. 1b show a core/shell distribution of phases. The core (interior) and shell consist of O3' and S phases, respectively, as expected from synthesis. High-angle annular dark-field (HAADF) STEM results confirm that the core/shell interface lies along $[010]_{O3'}/[110]_S$, with the spinel shell varying in thickness from 2 to 5 nm (Supplementary Fig. 1). O-*K* edge

electron energy-loss spectroscopy (EELS) shows an increase in pre-edge peak intensity from the shell to the interior (Supplementary Fig. 4a and b), suggesting a change in local O environment[28]. The Mn-$L_{2,3}$ edge shows a reduced Mn oxidation state in the shell, as evidenced by an increase in L_3/L_2 ratio (Supplementary Fig. 4c and d)[29], in agreement with the presence of a spinel layer.

Supplementary Fig. 5 shows an O3' phase orientation map, which highlights the presence of structural domains in the LMR oxide.[30,31] The domains are also revealed in the high-resolution HAADF-STEM shown in Fig. 1d. The bright–bright–dark contrast corresponds to TM–TM–Li ordering, which is characteristic of the O3' phase (see the inset to Fig. 1d). Three types of stacking of 'bright–bright–dark' contrast along $[001]_{O3'}$ form structural domains that are denoted A (green), B (blue) and C (pink). More details could be found in Supplementary Fig. 5a-c. Additional disordered structures visible in Figure 1e shows a diagrammatic representation of the types of structural domains in the O3' phase, which are in agreement with the observations.

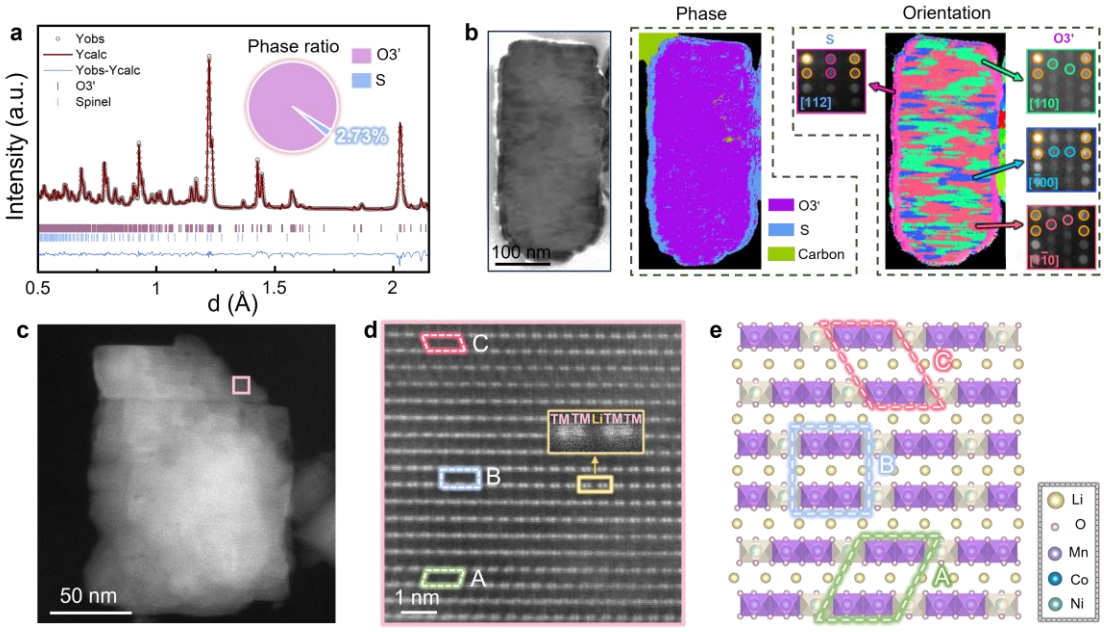

Fig. 1 | Initial structure of the LRM material. (**a**) NPD and Rietveld refinement analysis of pristine LRM powder. The inset sector plot shows the phase fraction distribution. (**b**) 4D-STEM results. Left to right: Virtual bright-field image, phase map and orientation map of a pristine LRM nanoparticle. Purple regions in the phase map denote the O3' phase, blue regions the

spinel phase and green regions amorphous C domains. (**c**) Low-magnification HAADF-STEM image of a pristine LRM particle. (**d**) High-resolution HAADF-STEM image of the marked area in (**c**), showing the atomic arrangement in the pristine LRM cathode, which exhibits structural domains in the O3' phase. The areas marked A (green), B (blue) and C (pink) correspond to domains projected along [110], [$\bar{1}$00] and [1$\bar{1}$0], respectively. (**e**) Schematic diagram of the O3' phase, showing different types of structural domains.

Phase evolution upon charge/discharge cycling

The structural evolution of the LRM oxide, which involves phase transitions, Li and TM ion migration and the release of O, poses severe challenges for conventional characterization methods. Whereas significant efforts have been made to study miniaturized coin half cells, the true conditions in a pouch cell are more complex, especially in an operational environment. Neutron diffraction offers sensitivity to light elements and the ability to distinguish elements with similar atomic numbers and different phases. The setup of the *operando* neutron diffraction experimental device used here is shown schematically in Supplementary Fig. 6a. In this configuration, incident neutrons interact with a pouch cell during a charge/discharge process and scattered neutrons are captured by annular detectors. A well-designed graphite || LRM pouch cell was prepared with 16 electrode layers and a gasbag (Supplementary Fig. 6b). The lattice parameters of the uncharged LRM oxide in the pouch cell are similar to those in the pristine powder (Supplementary Fig. 7 and Table 2), confirming that there is negligible influence from cell assembly and activation.

Figure 2a shows initial charge/discharge curves and two-dimensional plots of the evolution of neutron diffraction patterns as a function of time. The peaks marked by arrows are reflections from the LRM cathode. The pouch cell underwent a formation process before cycling (Supplementary Fig. 8). Then it was initially charged to 4.5 V at a current of 500 mA (1C ≈ 4000 mA), followed by a constant voltage charge at 4.5 V. It was then discharged to 2.5 V at a current of 500 mA. Despite some overlap of the reflections, in particular in the low-d region, most of the reflections from the cathode

and anode can be distinguished (Supplementary Fig. 9). Neutron diffraction patterns recorded from the pouch cell in the uncharged and fully-charged (4.5 V) states were analyzed to understand the transformations of the cathode material during the charge/discharge processes. Refined patterns for the two states are shown in Supplementary Fig. 10. The refinement considered layered structures of the O3' phase, the O3 phase (space group: $R\bar{3}m$) and the spinel structure. The goodness of fit confirms the precision of the calculated lattice structure of the LRM oxide.

Figure 2b shows the variation in phase fraction during the first cycle. During charging, the dominant O3' phase decreases gradually and almost completely transforms to the O3 phase at 4.5 V, as confirmed using phase mapping and atomic-resolution STEM (Supplementary Fig. 11). This transition is in agreement with previous findings.[32] However, the reverse transition is limited, with only half of the O3 phase returning to the O3' phase after discharging. We also observed this phenomenon in HAADF-STEM image of the cathode at 2.5 V (Supplementary Fig. 12). This limited reversibility results from the evolution of the LRM cathode during the first cycle and associated alterations in lattice structure. The proportion of the S phase also increases (Fig. 2b). The width of the S shell is approximately 5-10 nm in a fully charged particle, as shown in Supplementary Fig. 11b. The reduced intensity of the pre-edge peak in O *K*-edge spectra (Supplementary Fig. 13a and b) suggests that O vacancies accumulate in the S structure, in agreement with previous studies.[33,34]

Figure 2c shows the variation in $d_{intra\text{-}layer}$ and $d_{inter\text{-}layer}$ in the O3' and O3 phases with cycling time. As Li ions are extracted from the Li slabs, the shielding effect of electrostatic repulsion between adjacent TMO_2 slabs diminishes, increasing $d_{inter\text{-}layer}$ during charging. At the same time, $d_{intra\text{-}layer}$ contracts as a result of a reduction in ionic radius of the TM ions (most likely Ni and Co; see Supplementary Fig. 13c and d), which are oxidized to higher valence states. Above 4.4 V, the triggered O redox reaction partly counteracts the shielding effect, decelerating the variations in $d_{inter\text{-}layer}$ and $d_{intra\text{-}layer}$.[35] The increase in $d_{inter\text{-}layer}$ at the beginning of the discharge process may be attributed to

sluggish diffusion kinetics in the pouch cell for LRM materials, which also affects variations in $d_{intra\text{-}layer}$. The smaller changes in $d_{inter\text{-}layer}$ and $d_{intra\text{-}layer}$ during discharge can be explained by O reduction.

In order to obtain further insight into the irreversibility of the structural evolution of the LRM cathode from the neutron diffraction data (see Fig. 2d), the degree of honeycomb Li@TM_6 ordering (*DoO*) in the TMO_2 slab of the O3' phase is defined as follows:

$$DoO\ \ (\mathrm{Li@TM_6}) = \frac{Occ.(\mathrm{Li}, 2b)}{Occ.(\mathrm{Li}, 2b) + 2Occ.(\mathrm{Li}, 4g)} \times 100\%. \quad (1)$$

Figure 2e shows a fully-ordered Li@TM_6 superstructure in the O3' phase, in which only Li and only TM occupy 2*b* and 4g Wyckoff sites, respectively, *i.e.*, *DoO* (Li@TM_6) = 100%. This situation corresponds to the as-synthesized LRM in the pristine state. The degree of cation disordering (*DoD*) in the LiO_2 slab in the O3' phase is defined by the percentage of TM ions that migrate to 4*h* sites, as follows:

$$DoD\ \ (\mathrm{LiO_2}) = \frac{2Occ.(\mathrm{TM}, 4h)}{2Occ.(\mathrm{TM}, 4h) + 2Occ.(\mathrm{TM}, 4g) + Occ.(\mathrm{TM}, 2b)} \times 100\%. \quad (2)$$

During charging, *DoD* (LiO_2) increases gradually, while *DoO* (Li@TM_6) remains almost constant, suggesting that TM ions migrate from the TMO_2 to the Li slabs. When *DoD* (LiO_2) reaches ~1% (at 4.5 h), *DoO* (Li@TM_6) starts to decrease, suggesting that Li–TM reorganization takes place in the TMO_2 slabs. After charging to 4.5 V and during the entire discharging process, *DoO* (Li@TM_6) remains at ~50%, demonstrating a reduced degree of Li@TM_6 ordering (*e.g.*, 4*g* site: $TM_{0.75}Li_{0.25}$–$Li_{0.5}TM_{0.5}$) in the O3' phase (see Fig. 2d). Disorder between Li and TM in the TMO_2 and Li slabs most likely accounts for the irreversible transition from the O3' phase to the O3 phase. The increase in *DoD* (LiO_2) occurs after the formation of O vacancies:

$$0\ \mathrm{vacancy} = 0\ \mathrm{vacancy}(03') \times \mathrm{frac.}(03') + 0\ \mathrm{vacancy}(03) \times \mathrm{frac.}(03). \quad (3)$$

This behavior can be understood by the fact that O vacancies effectively lower the energy barrier associated with TM migration. The slight decrease in O vacancies during the discharge process suggests O reduction, as reported in the literature.[35] Similar results with regard to O variation are obtained from soft X-ray absorption spectroscopy, as shown in Supplementary Fig. 14.

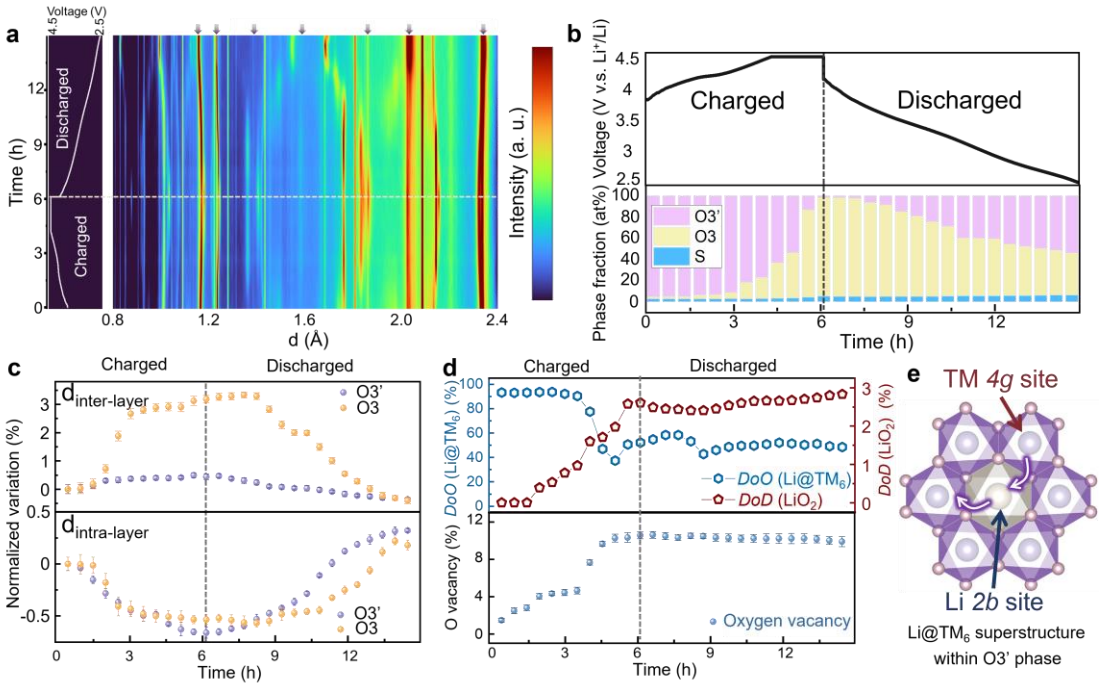

Fig. 2 | Structural evolution of the LRM cathode during the first cycle. (**a**) First charge/discharge curves of a graphite || LRM pouch cell and corresponding surface contour plot recorded using *operando* neutron diffraction. Contributions of LRM are marked by arrows. (**b**) Phase fraction evolution during the first cycle. Purple: O3'; yellow: O3; blue: spinel. (**c**) Values of $d_{inter\text{-}layer}$ and $d_{intra\text{-}layer}$ for the O3' and O3 phases in the LRM cathode obtained from Rietveld refinement as a function of cycling time. (In the hexagonal crystal system, $(0\ 0\ 3)_{O3}$ is equivalent to $(0\ 0\ 1)_{O3}$ in the monoclinic system. Therefore, $d_{inter\text{-}layer}$ corresponds to $d_{(0\ 0\ 3)_{O3}}$ and $d_{(0\ 0\ 1)_{O3'}}$. Similarly, $(1\ 0\ 0)_{O3}$, $(0\ 1\ 0)_{O3}$ and $(1\bar{1}\ 0)_{O3}$ are equivalent to $(1\ 3\ \overline{1/3})_{O3'}$, $(\bar{1}\ 3\ 1/3)_{O3'}$ and $(2\ 0\ \overline{2/3})_{O3'}$, respectively. Therefore, $d_{intra\text{-}layer}$ corresponds to $\left[d_{(1\ 0\ 0)_{O3}} + d_{(0\ 1\ 0)_{O3}} + d_{(1\ \bar{1}\ 0)_{O3}}\right] / 3$ in the O3 phase and to $\left[d_{(1\ 3\ \overline{1/3})_{O3'}} + d_{(\bar{1}\ 3\ 1/3)_{O3'}} + d_{(2\ 0\ \overline{2/3})_{O3'}}\right] / 3$ in the O3' phase. (**d**) Calculated ratio of *DoO* ($Li@TM_6$), *DoD* (LiO_2) and O vacancy plotted as a function of cycling time. (**e**) Schematic diagram of the $Li@TM_6$ superstructure in the O3' phase, in which Li and TM at

the TMO_2 slabs occupy 2*b* and 4*g* Wyckoff sites, respectively.

After 100 cycles (see Supplementary Fig. 15a), the LRM cathode comprises 72.02% of the O3 phase and 27.98% of the S phase (see Supplementary Fig. 15b and Supplementary Table 3), with no O3' phase detected after cycling. The thicker S shell (Supplementary Fig. 16a) results from the O3'→O3→S phase transition, which is associated with irreversible Li loss and an accumulation of O vacancies (Supplementary Fig. 14). Atomic-resolution STEM imaging along $<210>_{O3}$ (parallel to the O3' direction in Fig. 1d) reveals a completely disordered Li–TM arrangement (Supplementary Fig. 16b), without the characteristic O3' bright–bright–dark pattern that was present in the pristine sample.

Twinning-like structure evolution upon charge/discharge cycling

$<210>_{O3}$ projections allow structural phases and domains associated with $Li@TM_6$ ordering to be identified using STEM techniques (refer to Supplementary Fig. 5a – 5d). In order to further study microstructures associated with the TM stacking layers, we focus on $<100>_{O3}$ projections, along which Li and TM atoms line up (see Supplementary Fig. 5f and 5g). Figure 3 shows 4D-STEM orientation mapping of the microstructural evolution of LRM cathode particles upon cycling. Despite nanoscale intergrowth of O3' phase domains associated with $Li@TM_6$ ordering (Fig. 1), the pristine sample has a single-crystal-like microstructure (Fig. 3a). After a first charge to 4.5 V, a twinning-like microstructure is observed (Fig. 3b). The corresponding diffraction patterns are similar to those in Fig. 3c recorded from LRM particles after 100 cycles. The twinning structure generally develops further. The particles contain different orientations internally, with a significant fraction terminating in the particle, rather than extending across it. The results show that defects such as dislocations and stacking faults form primarily towards the end of the cycle. Diffraction patterns extracted from two areas (right part of Fig. 3c) have mirror symmetry, which is consistent with twin-like structures in the purple and yellow regions. As the resolution of the 4D-STEM technique was ~2 nm, finer structures could not be resolved.

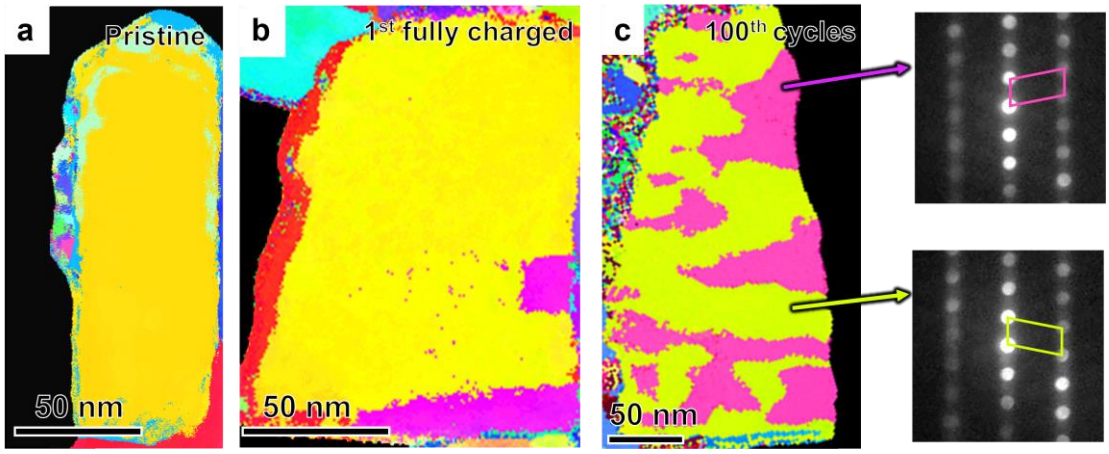

Fig. 3 | LRM structure evolution viewed along the <100>$_{O3}$ projection. (**a-c**) In-plane orientation mapping of (**a**) a pristine particle, (**b**) a particle after a first charge to 4.5 V and (**c**) a particle after 100 cycles. The diffraction patterns were obtained from the purple and yellow areas in (**c**), which have mirror symmetry. The corresponding diffraction patterns of yellow and purple areas in (b) are familiar with those in (c). Note that in the pristine state, the particle is dominated by O3' phase, its orientation relationship with O3 is given in Supplementary Fig. 5.

Figures 4a, b shows low-magnification and magnified HAADF-STEM images of an LRM nanoparticle as it was initially charged to 4.5 V. The (acute) angles between the TM stacking layers vary, forming twinning-like structures (marked in blue and orange). The angles in neighboring variants are ~79° and ~83°. Regions of O1-type structure, which are identified by a 90°angle between the TM stacking layers (marked in green), typically have widths of below 2 nm (Supplementary Fig. 17a), which is beyond the present orientation mapping detection limit. Such structures have also been observed in delithiation Ni-rich cathodes.[36] In comparison with an O1-type structure, twinning-like structures present greater challenges for Li^+ accommodation in layer-structured Li-ion battery materials, hindering reversible Li^+ intercalation.[36]

Atomic-resolution detail from the area outlined in cyan in Fig. 4b was analyzed quantitatively. Image noise was removed using a nonlinear algorithm and atomic positions were measured using 2D Gaussian fitting.[37] The ratio m/n between the two diagonals in each unit cell was determined based on the measured positions for tracing the structural variations. The result is shown in Fig. 4c. Two types of microstructures

are highlighted: 1) A twinning-like structure (region I) and an O1/O3 boundary (region II), forming coherent interlayer microstructures with an $(001)_{O3}$ habit plane. This twinning is called intralayer coherent twinning (refer to Supplementary Fig. 18). The *m*/*n* ratio in region I is ~0.85 and ~1.15 for the blue and magenta variant, respectively; 2) Local structural frustrations in regions III and IV, which are indicative of intralayer microstructures and can be traced by extending the blue and magenta twinning variants in the magnified images (see the double-headed arrows). In this type of twinning structure, the $\{012\}_{O3}$ twinning boundary (TB) is incoherent (so-called intralayer incoherent twinning). In the same layer, transitional interfaces that form a quasi-twinned structure are not continuous. When adjacent twinning variants meet at TB, structural frustration forms, as illustrated in Supplementary Fig. 18. Similar structures were previously observed in a Ni-rich cathode.[36] The presence of intralayer frustration is indicative of nanoscale charge heterogeneity in fully-charged particles. More similar structures were observed, as shown in Supplementary Fig. 17. And mapping of interlayer spacings (Supplementary Fig. 17b) shows an uneven lattice distribution after charging, indicating a non-uniform delithiation process, with expansion and contraction of the interlayers. Strain measurement using geometric phase analysis reveals significant strain accumulation in the vicinity of a frustrated interface (Supplementary Fig. 19).[38] In subsequent cycles, such frustrated structures may be prone to strain relaxation, leading to structural failure.

The atomic structures in the LRM cathode after 100 electrochemical cycles are shown in Fig 4d-g. Both interlayer and intralayer microstructures have developed further. Similarly to Fig. 4b, the interlayer microstructures maintain their coherence between neighboring twinning variants, while the intralayer interfaces expand in the $\{012\}_{O3}$ habit planes. The density of intralayer interfaces (Supplementary Fig. 20, Supplementary Table 4) is ~5 per particle. Strikingly, pore-like structures form at the $\{012\}_{O3}$ twinning interface due to the expansion of local intralayer frustrations, leading to lattice bending and reduced atomic connectivity, as revealed in Fig. 4e, f. The Fast Fourier Transform (FFT) of the high-resolution image reveals a twinning-like structure

(Fig. 4g). The formed pore-like interface microstructures, which resembling trenches, are believed to block Li^+ diffusion during charge-discharge operations, reducing Li delithiation-lithiation and resulting in fading of battery capacity with cycling. Additionally, the EELS and EDS measurements were conducted in the defect and normal area. The spectrum in Supplementary Fig. 21 showed that the Mn concentration in the defect region is lower than that in the normal region, and valance of Mn in defect region is Mn^{3+}, while it is $Mn^{3.5+}$ in the normal region. These results revealed the dissolution and migration of Mn in the defect area during cycling, which is consistent with the results from the neutron diffraction.

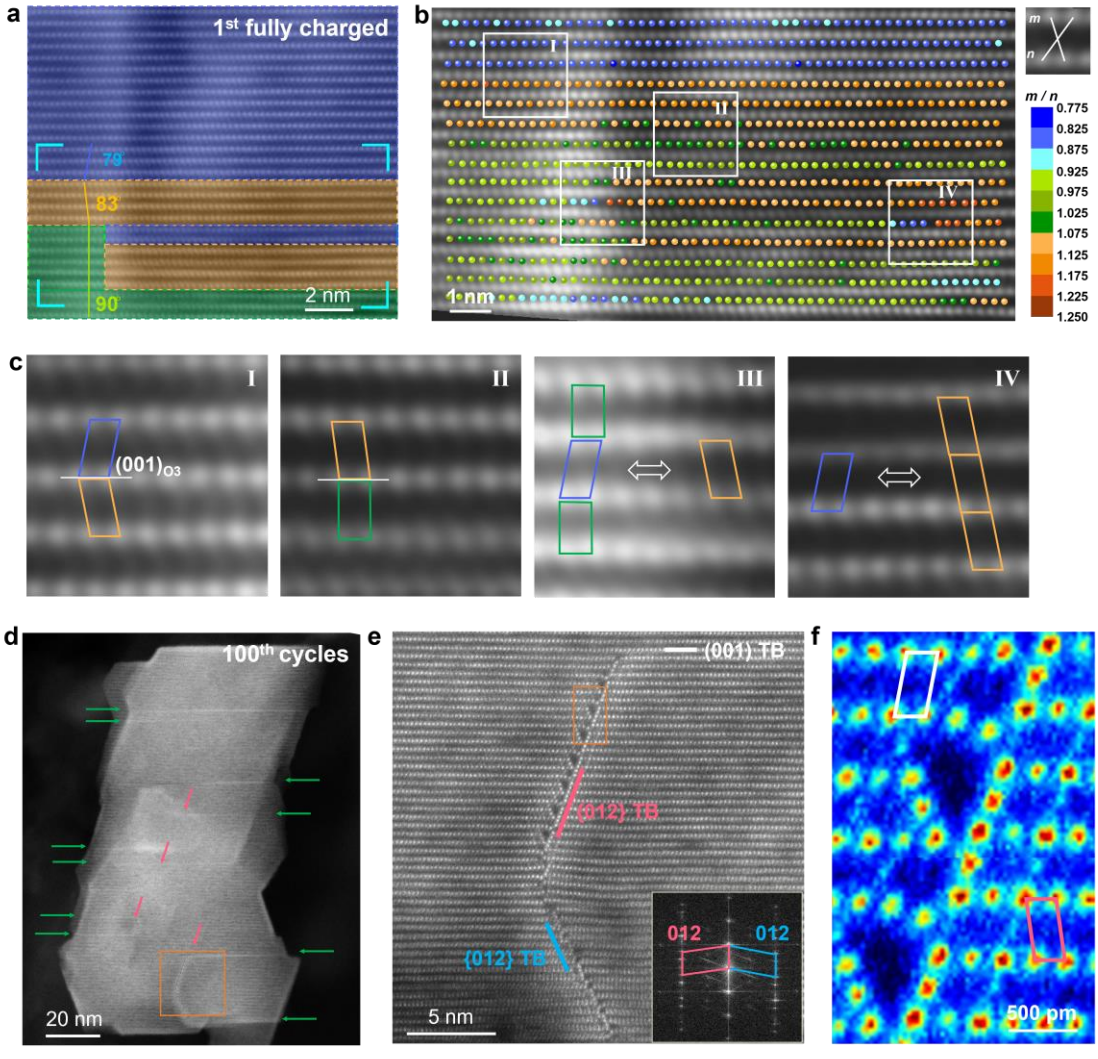

Fig. 4 | LRM structure after cycling. (**a**) Atomic-resolution image of a representative region viewed along $<100>_{O3}$, showing changes to angles for the cathode charged to 4.5 V. (**b**) The unit-cell-by-unit-cell microstructural changes corresponding to the cyan area in (**a**), defined by

the ratio *m/n*, where *m* and *n* are diagonal distance of the unit cell. (**c**) Magnified versions of areas I-IV in (**b**). (**d**) HAADF-STEM image showing an overview of a representative particle after 100 cycles. The interlayer and intralayer twinning boundaries are marked by green and orange arrows. (**e**) Atomic-resolution image of the area marked in (**d**), showing the interlayer (001) coherent twinning boundary and intralayer {012} incoherent twinning boundaries. The inset shows an FFT of (e), which confirms the presence of a twinning-like structure (see Supplementary Fig.18). (**f**) High-resolution image of the area marked in (**e**), showing pore-like microstructures resulted from the intralayer twinning mediated frustration. The twinning variants are indicated by the white and pink frames.

Discussion

Based on our experimental observations, the phase evolution of LRM cathodes is shown schematically in Fig. 5a. During charging, as Li ions are extracted from the Li layer, Li ions in the TM layer also migrate to the Li layer. At high voltage, anion oxidation drives rearrangement in the TM layer, which contains Li vacancies, leading to the formation of O clusters that facilitate oxidation of O^{2-} into O_2.[21] This is an irreversible redox pathway for O, resulting in voltage hysteresis during discharge. Therefore, minimizing or preventing the rearrangement of TM ions within the TM-layers can effectively address the issue of voltage hysteresis during electrochemical processes. In the context of Li-Mn-based sodium-ion cathodes, optimizing the ordered superlattice of Li and TM within the TM-layers has proven to be an effective strategy for suppressing TM rearrangement, thereby reducing voltage hysteresis.[21] As Li ions are reinserted into the Li layer during discharge, some of them migrate back into the TM layer. However, as a result of the mixed distribution in the TM layer, the ordered structure of the O3' phase is disrupted, resulting in partial transformation of the O3' phase into the O3 phase. This transformation proceeds irreversibly during continued cycling, reducing the cell capacity. Nevertheless, this phase transition may not be the primary reason for performance degradation, as cathodes with pure S or O3 phases still have some capacity.[14] Instead, expansion of the intralayer microstructures is most likely to be responsible for electrochemical performance decay.

As shown in Fig. 5b, a large number of TM and O vacancies form in the TM layer, together with irreversible migration of Li and the release of O. Lithium, transition metal, and oxygen vacancies may result in localized vacancy loops, [39] which develop into the observed defects extending over the whole nanoparticle. According to the previous report, the dislocations formed more readily in Li-rich cathode as compared with a classical layered oxide. [39] Similarly, we posit that interlayer slips of TM layers occur during electrochemical cycling, forming two types of twinning-like structures, one is interlayer coherent twinning, and the other one is intralayer incoherent twinning, and O1/O3 boundaries. The structural frustration forms when these twinning variants meet at the twinning boundary. As cycling progresses, the interlayer twinning-like structures maintain their coherence between neighboring twinning variants, while the intralayer TBs expand in the $\{012\}_{O3}$ habit planes. More prominent frustration is evidenced by the formation of local pore-like microstructures (or trenches) at the $\{012\}_{O3}$ TBs, as shown in Figure 4 and Supplementary Fig. 22. The formation of pore-like interface microstructures reduces atomic connectivity and hinders Li^+ diffusion from the bulk to the surface. We proposed that TM ions irreversible migration plays an important role for the structure and performance failure in LRM oxides. Introducing pinning TMs above central Li^+ sites in the $Li@TM_6$ honeycomb superstructure might be an effective approach to stabilize Li^+ within the TM layer and prevent interlayer migration, thereby achieving low voltage and capacity fade.[7]

Surface reconstruction is also a crucial factor for material failure.[40] Our work considers surface effects by modifying the particle surfaces with a spinel layer to reduce O release and to minimize the generation of side reactions during cycling. Although the surface spinel phase thickens during extended cycling, it does not prevent material failure due to changes in inner bulk structure and degradation in material performance results primarily from intrinsic structural changes. Our findings suggest that coating or surface modification methods may help to inhibit surface degradation, but are likely to be insufficient to prevent capacity fade because nanoscale defect formation can proceed from the particle interior. Modification of the bulk structure, for example by anchoring

TM ions in the TM layer to suppress their inter-/intra-layer migration, should be considered to stabilize the structures of Li-rich cathodes for improved electrochemical performance. The above discussion further guided the optimization of Li-rich oxide cathodes, which was provided in Supplementary Fig. 23.

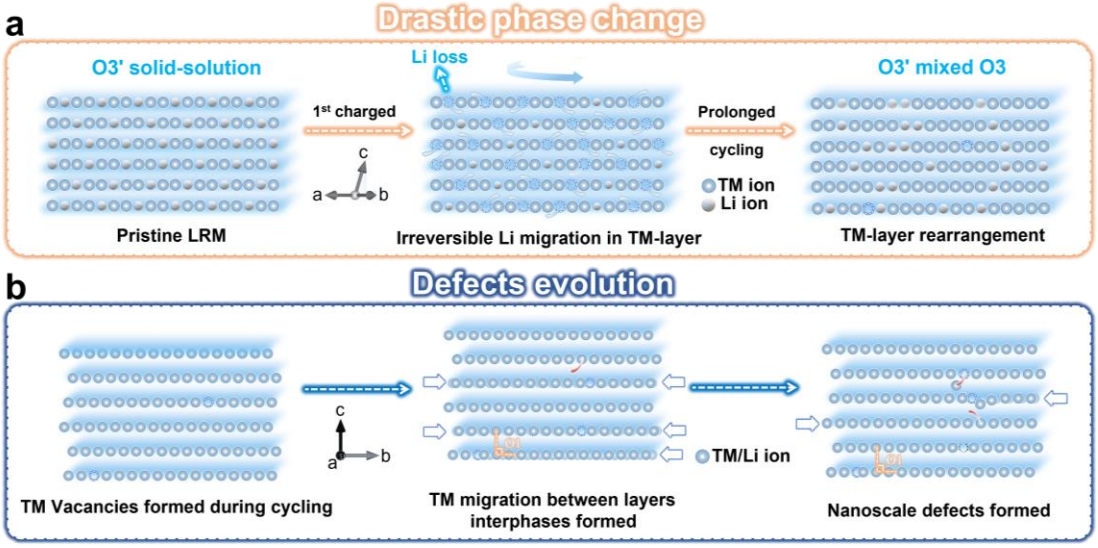

Fig. 5 | Evolution process of nanoscale defects and TM migration. (**a**) Schematic diagram of phase evolution. (**b**) Schematic diagram of the correlation between defects and TM migration.

In summary, a combination of STEM and *operando* neutron diffraction techniques has been used to reveal the relationship between microstructure and performance in LMR cathodes across different length scales. Synthesized pristine LRM particles are shown to comprise a solid solution, with Li@TM_6 ordering based on *C2/m* symmetry (O3' type) surrounded by a thin spinel shell. It transitions from an ordered monoclinic phase to a disordered rhombohedral phase as a result of irreversible Li ion migration and transition metal rearrangement during cycling. During initial cycling, the irreversible extraction of Li ions from transition metal layers leads to the formation of the interlayer (001) twinning-like structures and local intralayer frustrations formed in the material. During subsequent extended cycles, the intralayer frustrations further develop into pore-like structure along {012} twinning boundary in the bulk of the particles with the continuous loss of Li ions and the migration of transition metal ions in the layers. These defects obstruct channels for Li-ion transport in the layers, causing a deterioration in material

performance. These observations provide a perspective on material failure mechanisms in layered high-energy cathodes and emphasize the importance of intrinsic modification methods for stabilizing their internal structures beyond surface modification.

Methods

Material synthesis

The cathode precursor $Mn_{2/3}Co_{1/6}Ni_{1/6}CO_3$ was synthesized by a co-precipitation method. First, 2.0 mol/L $MnSO_4·4H_2O$ (Aladdin, 99.9%), $NiSO_4·6H_2O$ (Aladdin, 99.9%) and $CoSO_4·7H_2O$ (Aladdin, 99.9%) solutions were stirred in the reactor. Meanwhile, 2.0 mol/L Na_2CO_3 (Aladdin, 99.9%) and NH_4OH solution (Aladdin, 500 mg/L) were added to the reactor separately. The stirring temperature was kept at 60 °C at a fixed pH value of 7.8. The precursor powders were obtained after washing several times with deionized water and dried in vacuum at 80 °C for 12 h. The precursor was then well ground with Li_2CO_3 (Aladdin, 99.9%) (5% excess). Subsequently, the obtained mixture was transferred to a furnace, calcined at 480 °C for 5 h and heated to 850 °C for 12 h in air. The untreated $Li_{1.2}Mn_{0.54}Ni_{0.13}Co_{0.13}O_2$ (u-LRM) was obtained. Then the synthesized LRM with a thin spinel-layer product was obtained after re-sintering for 3 h at a heating speed of 2℃ min from room temperature to 400℃ in an Ar atmosphere. The synthesized samples were stored in an Ar-filled glovebox (Mikrouna Super 1220) with O_2 and H_2O contents of below 0.01 ppm.

Half-cell preparation

The synthesized u-LRM or LRM material, which served as the active material for the half-cell cathode, was mixed with acetylene black (C45 Conductive Carbon Black, TIMCAL) and poly-(vinylidene fluoride) (PVDF) (Aladdin, K30) in the ratio 8:1:1 (wt%) in N-methyl-2-pyrrolidone (NMP) (Aladdin, 99.5%) solvent to form a homogeneous slurry. This slurry was uniformly coated on a 40-μm-thick aluminum foil and dried in an oven at 80 °C for 2 h. The preliminarily dried electrode sheet was cut into circular pieces of diameter 12 mm, ensuring a loading of active material per single

sheet of at least 2 mg cm^{-2}. These electrode sheets were placed in a vacuum oven at 110 °C for 12 h to remove the solvents and any residual moisture. The dried electrode sheets were stored in an Ar-filled glovebox (Mikrouna Super 1220) with O_2 and H_2O contents of below 0.01 ppm. The anode of the half-cell utilized a pure Li metal foil (16 mm diameter, 0.6 mm thickness, 99.9% purity) and a polypropylene separator (25 μm, Celgard 2500). The electrolyte utilized was 1 M $LiPF_6$ dissolved in a mixed solution of 1,1,2,2-tetrafluoroethyl-2′,2′,2′-trifluoroethyl, methyl (2,2,2-trifluoroethyl) carbonate and fluoroethylene carbonate (2:6:2, wt%). The assembly of coin-type half-cells (2032) was performed in the same glovebox.

Pouch cell preparation

The LRM cathode material was dispersed homogeneously in NMP with acetylene black and PVDF in a precise ratio of 9:0.5:0.5 (wt%) to form a well-mixed slurry. This slurry was coated onto Al foil (145 mm × 75 mm). The graphite anode material was dissolved in NMP, incorporating acetylene black and PVDF in the same ratio, to generate a slurry that was coated onto Cu foil (145 mm × 75 mm). The capacity of anode exceeded that of the LRM cathode. Pouch cell assembly was carried out meticulously in a glovebox, including integration of the cathode, anode, separator and electrolyte. In order to enhance loading of the active materials and to optimize the neutron diffraction patterns, the cathode and anode materials were coated uniformly on both sides of the Al foil and Cu foil. The resulting cell configuration comprised 16 pieces of dual-sided LRM cathode and graphite anode. A Celgard separator was used to alternate coverage of the anode and cathode on each side. The electrolyte utilized was the same as for the half cell. The assembly of pouch cell was performed in the same glovebox.

Electrochemical tests

Half cell: Cyclic voltammetry (CV) measurements were conducted using an OCTOSTAT200 electrochemical workstation (IVIUM Instrument) in the voltage range 2 - 4.8 V versus Li^+/Li at room temperature with a scan rate of 0.1 mV s^{-1}. Galvanostatic charge/discharge (GCD) tests were carried out on a Landt Instruments battery cycler at

specific current densities (1 C = 250 mA g^{-1}) in the voltage window 2.0 - 4.8 V versus Li^+/Li at 30 °C.

Pouch cell: The pouch cell was designed with a standard capacity of 4 Ah. Initially, the as-prepared pouch cell underwent a formation process, charging to 4.5 V at increasing currents of 250 mA, 500 mA and 1000 mA, in order to ensure complete electrolyte infiltration into the cathode, anode and separator of the pouch cell. Subsequently, the activated pouch cell was used for *operando* neutron diffraction experiments. The final analysis of the failed LRM structure was conducted based on the pouch cell after 100 cycles at 4000 mA in the voltage range 2.5 - 4.5 V.

Neutron powder diffraction and *operando* neutron diffraction

Neutron powder diffraction experiments were carried out on the Time-of-Flight (TOF) diffractometer Multi-Physics Instrument (MPI) of the China Spallation Neutron Source (CSNS). Charge and discharge tests of the pouch cell were conducted using a battery cycler (Landt Instruments) with a constant current of 400 mA for the first cycle. TOF neutron diffraction data for *in operando* pouch cell analysis were acquired on the General Purpose Powder Diffractometer (GPPD) at the CSNS in Dongguan, China. An incident neutron beam with a wavelength band ranging from 0.1 to 4.9 Å was used. Real-time neutron diffraction data were collected while the pouch cell underwent charge and discharge processes. The crystal structures of the electrodes were determined through Rietveld refinement using the FullProf program.

HAADF and 4D-STEM data collection

In order to prepare samples for transmission electron microscopy, the electrodes were washed after cycling using dimethyl carbonate and dried in an Ar-filled glovebox. Both the pristine cathodes and the cathodes after cycling were ultrasonicated in ethanol for 15 min and dispersed on Cu TEM grids for characterization. The electrodes were then ultrasonicated in ethanol and dispersed on the Cu TEM grids.

Electron microscopy techniques, including HAADF imaging and EELS, were

performed at 200 kV on an FEl Titan G2 ChemiSTEM 80-200 transmission electron microscope equipped with a high-brightness field emission gun and a probe spherical aberration (Cs) correction system. Atomic-resolution HAADF-STEM images were acquired in STEM mode using a high-angle annular dark-field detector. The convergence semi-angle for HAADF imaging was ~25 mrad, while the collection semi-angle was ~70-200 mrad. EEL spectra were acquired in STEM mode. The convergence semi-angle was the same as for HAADF imaging.

4D-STEM experiments were conducted on a Tescan Tensor precession-assisted 4D-STEM microscope, which can perform near-real-time analysis and processing of 4D-STEM data, using a convergence semi-angle of 1.5 mrad, a beam current of 200 pA, a probe size of 1.5 nm. a diffraction size of 124.5 mrad and a precession angle of 0.8°. The electron probe was raster-scanned across NPs using a 2 nm step size. A diffraction pattern was recorded at each probe position using a high-performance hybrid-pixel direct electron diffraction camera (Dectris Quadro) with 512 × 512 physical pixels using 4-fold binning (128 × 128 pixels) and an exposure time of 3 ms for each pixel.

Synchrotron soft X-ray absorption spectroscopy

After the pouch cells had been charged and discharged to the target states, they were disassembled in the Ar-filled glovebox. The cathode components were extracted, subjected to thorough cleaning with a dimethyl carbonate (DMC) solution and dried. O K-edge absorption spectra were recorded meticulously from various LRM states in the RGBL beamline station at BESSY-II, Germany in fluorescence yield (FY) mode.

Data Availability

Data that support the findings of this study are available from the corresponding author on request.

References

1 Whittingham, M. S. Lithium Batteries and Cathode Materials. *Chemical Reviews* **104**, 4271-4302, doi:10.1021/cr020731c (2004).

2 Li, M., Lu, J., Chen, Z. & Amine, K. 30 Years of Lithium-Ion Batteries. *Advanced Materials* **30**, 1800561, doi:https://doi.org/10.1002/adma.201800561 (2018).
3 Wang, L., Liu, T., Wu, T. & Lu, J. Strain-retardant coherent perovskite phase stabilized Ni-rich cathode. *Nature* **611**, 61-67, doi:10.1038/s41586-022-05238-3 (2022).
4 Liu, J. *et al.* Recent breakthroughs and perspectives of high-energy layered oxide cathode materials for lithium ion batteries. *Materials Today* **43**, 132-165, doi:https://doi.org/10.1016/j.mattod.2020.10.028 (2021).
5 Liu, T. *et al.* Origin of structural degradation in Li-rich layered oxide cathode. *Nature* **606**, 305-312, doi:10.1038/s41586-022-04689-y (2022).
6 Seo, D.-H. *et al.* The structural and chemical origin of the oxygen redox activity in layered and cation-disordered Li-excess cathode materials. *Nature Chemistry* **8**, 692-697, doi:10.1038/nchem.2524 (2016).
7 Luo, D. *et al.* A Li-rich layered oxide cathode with negligible voltage decay. *Nature Energy* **8**, 1078-1087, doi:10.1038/s41560-023-01289-6 (2023).
8 Zuo, Y. *et al.* A High-Capacity O2-Type Li-Rich Cathode Material with a Single-Layer Li2MnO3 Superstructure. *Advanced Materials* **30**, 1707255, doi:https://doi.org/10.1002/adma.201707255 (2018).
9 Zuo, W. *et al.* Li-rich cathodes for rechargeable Li-based batteries: reaction mechanisms and advanced characterization techniques. *Energy & Environmental Science* **13**, 4450-4497, doi:10.1039/D0EE01694B (2020).
10 Zuo, Y. *et al.* Regulating the Potential of Anion Redox to Reduce the Voltage Hysteresis of Li-Rich Cathode Materials. *Journal of the American Chemical Society* **145**, 5174-5182, doi:10.1021/jacs.2c11640 (2023).
11 Li, N. *et al.* Enabling Facile Anionic Kinetics through Cationic Redox Mediator in Li-Rich Layered Cathodes. *ACS Energy Letters* **5**, 3535-3543, doi:10.1021/acsenergylett.0c01880 (2020).
12 Hao, Z. *et al.* Suppressing Bulk Strain and Surface O_2 Release in Li-Rich Cathodes by Just Tuning the Li Content. *Advanced Materials* **36**, 2307617, doi:https://doi.org/10.1002/adma.202307617 (2024).
13 Kim, S. Y. *et al.* Inhibiting Oxygen Release from Li-rich, Mn-rich Layered Oxides at the Surface with a Solution Processable Oxygen Scavenger Polymer. *Advanced Energy Materials* **11**, 2100552, doi:https://doi.org/10.1002/aenm.202100552 (2021).
14 Mohanty, D. *et al.* Unraveling the Voltage-Fade Mechanism in High-Energy-Density Lithium-Ion Batteries: Origin of the Tetrahedral Cations for Spinel Conversion. *Chemistry of Materials* **26**, 6272-6280, doi:10.1021/cm5031415 (2014).
15 Song, J. *et al.* Entropy Stabilization Strategy for Enhancing the Local Structural Adaptability of Li-Rich Cathode Materials. *Advanced Materials* **35**, 2208726, doi:https://doi.org/10.1002/adma.202208726 (2023).
16 Cui, C. *et al.* Structure and Interface Design Enable Stable Li-Rich Cathode. *Journal of the American Chemical Society* **142**, 8918-8927, doi:10.1021/jacs.0c02302 (2020).
17 Guo, W. *et al.* Enhancing cycling stability in Li-rich Mn-based cathode materials by solid-liquid-gas integrated interface engineering. *Nano Energy* **97**, 107201, doi:https://doi.org/10.1016/j.nanoen.2022.107201 (2022).
18 Kim, S., Cho, W., Zhang, X., Oshima, Y. & Choi, J. W. A stable lithium-rich surface

546 structure for lithium-rich layered cathode materials. *Nature Communications* **7**, 13598,
547 doi:10.1038/ncomms13598 (2016).
548 19 Ye, Z. *et al.* A Simple Gas–Solid Treatment for Surface Modification of Li-Rich Oxides
549 Cathodes. *Angewandte Chemie International Edition* **60**, 23248-23255,
550 doi:https://doi.org/10.1002/anie.202107955 (2021).
551 20 Yang, J. *et al.* Suppressing Voltage Fading of Li-Rich Oxide Cathode via Building a
552 Well-Protected and Partially-Protonated Surface by Polyacrylic Acid Binder for Cycle-
553 Stable Li-Ion Batteries. *Advanced Energy Materials* **10**, 1904264,
554 doi:https://doi.org/10.1002/aenm.201904264 (2020).
555 21 House, R. A. *et al.* The role of O_2 in O-redox cathodes for Li-ion batteries. *Nature*
556 *Energy* **6**, 781-789, doi:10.1038/s41560-021-00780-2 (2021).
557 22 Csernica, P. M. *et al.* Persistent and partially mobile oxygen vacancies in Li-rich
558 layered oxides. *Nature Energy* **6**, 642-652, doi:10.1038/s41560-021-00832-7 (2021).
559 23 House, R. A. *et al.* First-cycle voltage hysteresis in Li-rich 3d cathodes associated with
560 molecular O_2 trapped in the bulk. *Nature Energy* **5**, 777-785, doi:10.1038/s41560-020-
561 00697-2 (2020).
562 24 Huang, J. *et al.* Inhibiting collective cation migration in Li-rich cathode materials as a
563 strategy to mitigate voltage hysteresis. *Nature Materials* **22**, 353-361,
564 doi:10.1038/s41563-022-01467-z (2023).
565 25 Pearce, P. E. *et al.* Evidence for anionic redox activity in a tridimensional-ordered Li-
566 rich positive electrode β-Li_2IrO_3. *Nature Materials* **16**, 580-586,
567 doi:10.1038/nmat4864 (2017).
568 26 Yin, C. *et al.* Structural insights into composition design of Li-rich layered cathode
569 materials for high-energy rechargeable battery. *Materials Today* **51**, 15-26,
570 doi:https://doi.org/10.1016/j.mattod.2021.10.020 (2021).
571 27 Ophus, C. Four-Dimensional Scanning Transmission Electron Microscopy (4D-
572 STEM): From Scanning Nanodiffraction to Ptychography and Beyond. *Microscopy*
573 *and Microanalysis* **25**, 563-582, doi:10.1017/S1431927619000497 (2019).
574 28 Li, L. *et al.* Hidden Subsurface Reconstruction and Its Atomic Origins in Layered
575 Oxide Cathodes. *Nano Letters* **20**, 2756-2762, doi:10.1021/acs.nanolett.0c00380
576 (2020).
577 29 Tan, H., Verbeeck, J., Abakumov, A. & Van Tendeloo, G. Oxidation state and chemical
578 shift investigation in transition metal oxides by EELS. *Ultramicroscopy* **116**, 24-33,
579 doi:https://doi.org/10.1016/j.ultramic.2012.03.002 (2012).
580 30 Jarvis, K. A., Deng, Z., Allard, L. F., Manthiram, A. & Ferreira, P. J. Atomic Structure
581 of a Lithium-Rich Layered Oxide Material for Lithium-Ion Batteries: Evidence of a
582 Solid Solution. *Chemistry of Materials* **23**, 3614-3621, doi:10.1021/cm200831c (2011).
583 31 Liu, H. *et al.* Unraveling the Rapid Performance Decay of Layered High-Energy
584 Cathodes: From Nanoscale Degradation to Drastic Bulk Evolution. *ACS Nano* **12**,
585 2708-2718, doi:10.1021/acsnano.7b08945 (2018).
586 32 Jiang, Y.-s. *et al.* Revealing the Thermodynamics and Kinetics of In-Plane Disordered
587 Li_2MnO_3 Structure in Li-Rich Cathodes. *ACS Energy Letters* **6**, 3836-3843,
588 doi:10.1021/acsenergylett.1c01904 (2021).
589 33 Yu, L., Huang, Y., Han, Q., Zhu, J. & Lu, J. High Cycling Rate-Induced Irreversible

TMO6 Slabs Glide in Co-Free High-Ni Layered Cathode Materials. *Advanced Functional Materials* **33**, 2301650, doi:https://doi.org/10.1002/adfm.202301650 (2023).

34 Wang, R. *et al.* Constructing oxygen-deficient shell on Li-rich cathodes by spark plasma sintering for high-performance lithium-ion batteries. *Next Materials* **4**, 100195, doi:https://doi.org/10.1016/j.nxmate.2024.100195 (2024).

35 Zhou, Y. *et al.* Sufficient Oxygen Redox Activation against Voltage Decay in Li-Rich Layered Oxide Cathode Materials. *ACS Materials Letters* **3**, 433-441, doi:10.1021/acsmaterialslett.1c00088 (2021).

36 Wang, C. *et al.* Resolving complex intralayer transition motifs in high-Ni-content layered cathode materials for lithium-ion batteries. *Nature Materials* **22**, 235-241, doi:10.1038/s41563-022-01461-5 (2023).

37 Du, H. A nonlinear filtering algorithm for denoising HR(S)TEM micrographs. *Ultramicroscopy* **151**, 62-67, doi:https://doi.org/10.1016/j.ultramic.2014.11.012 (2015).

38 Hÿtch, M. J., Snoeck, E. & Kilaas, R. Quantitative measurement of displacement and strain fields from HREM micrographs. *Ultramicroscopy* **74**, 131-146, doi:https://doi.org/10.1016/S0304-3991(98)00035-7 (1998).

39 Singer, A. *et al.* Nucleation of dislocations and their dynamics in layered oxide cathode materials during battery charging. *Nature Energy* **3**, 641-647, doi:10.1038/s41560-018-0184-2 (2018).

40 Yan, P. *et al.* Evolution of Lattice Structure and Chemical Composition of the Surface Reconstruction Layer in $Li_{1.2}Ni_{0.2}Mn_{0.6}O_2$ Cathode Material for Lithium Ion Batteries. *Nano Letters* **15**, 514-522, doi:10.1021/nl5038598 (2015).

Acknowledgements

This work was supported financially by the National Key R&D Program of China (2020YFA0406203), Research Infrastructure Access in Nanoscience & Nanotechnology (RIANA) project, funded by the European Union (101130652), National Natural Science Foundation of China (No. 92472115 and No. 52072008), Guangdong Basic and Applied Basic Research Foundation (No. 2022B1515120070 and No. 2022A1515110816), the Large Scientific Facility Open Subject of Songshan Lake, Dongguan, Guangdong (No. KFKT2022A04) and the Major Science and Technology Infrastructure Project of Material Genome Big-Science Facilities Platform supported by the Municipal Development and Reform Commission of Shenzhen. The authors are grateful for neutron beam time at MPI and GPPD granted by CSNS, Dongguan, China. Lunhua He, Jie Chen, Sihao Deng, Huaile Lu, Zhijian Tan, Feiran Shen and Yaoda Wu are thanked for technical assistance with the operando neutron diffraction experiments.

Ziqin Jiao, Xiaoyu Gao are thanked for the supporting with the materials synthesis. Wen Yin, Yuanguang Xia and Juping Xu are thanked for technical assistance with the powder neutron diffraction experiments. The authors also thank the Tescan Tensor STEM team for their technical assistance during 4D-STEM experiments.

Author Contributions

T. Y., M. Y., L. J. and Y. X. conceived the idea and designed the experiments. M. Y., R. W., Z. L. and J. W. prepared the pouch cell and conducted the electrochemical measurements. Z. H. and R. W. carried out the *operando* neutron diffraction measurements. M. Y. and Z. H. completed Rietveld refinement of all diffraction data. T. Y. P. L. and J. L. carried out 4D-STEM, STEM and EELS measurements and data analysis. M. Y., T. Z. and W. J. performed *ex situ* sXAS tests and data analysis. T. Y., M. Y., Z. H., L. J., R. D. and Y. X. participated in the mechanism discussions. T. Y., M. Y., L. J., R. D. and Y. X. wrote the manuscript. All of the authors discussed the results and edited the manuscript.

Competing Interests

The authors declare no competing interests.

Figure Captions

Fig. 1 | Initial structure of the LRM material. (**a**) NPD and Rietveld refinement analysis of pristine LRM powder. The inset sector plot shows the phase fraction distribution. (**b**) 4D-STEM results. Left to right: Virtual bright-field image, phase map and orientation map of a pristine LRM nanoparticle. Purple regions in the phase map denote the O3' phase, blue regions the spinel phase and green regions amorphous C domains. (**c**) Low-magnification HAADF-STEM image of a pristine LRM particle. (**d**) High-resolution HAADF-STEM image of the marked area in (**c**), showing the atomic arrangement in the pristine LRM cathode, which exhibits structural domains in the O3' phase. The areas marked A (green), B (blue) and C (pink) correspond to domains projected along [110], [$\bar{1}$00] and [1$\bar{1}$0], respectively. (**e**) Schematic diagram of the O3' phase, showing different types of structural domains.

Fig. 2 | Structural evolution of the LRM cathode during the first cycle. (**a**) First charge/discharge curves of an graphite || LRM pouch cell and corresponding surface contour plot recorded using *operando* neutron diffraction. Contributions of LRM are marked by arrows. (**b**) Phase fraction evolution during the first cycle. Purple: O3'; yellow: O3; blue: spinel. (**c**) Values of $d_{\text{inter-layer}}$ and $d_{\text{intra-layer}}$ for the O3' and O3 phases in the LRM cathode obtained from Rietveld refinement as a function of cycling time. (In the hexagonal crystal system, $(0\ 0\ 3)_{O3}$ is equivalent to $(0\ 0\ 1)_{O3}$ in the monoclinic system. Therefore, $d_{\text{inter-layer}}$ corresponds to $d_{(0\ 0\ 3)_{O3}}$ and $d_{(0\ 0\ 1)_{O3'}}$. Similarly, $(1\ 0\ 0)_{O3}$, $(0\ 1\ 0)_{O3}$ and $(1\bar{1}\ 0)_{O3}$ are equivalent to $(1\ 3\ \overline{1/3})_{O3'}$, $(\bar{1}\ 3\ 1/3)_{O3'}$ and $(2\ 0\ \overline{2/3})_{O3'}$, respectively. Therefore, $d_{\text{intra-layer}}$ corresponds to $\left[d_{(1\ 0\ 0)_{O3}} + d_{(0\ 1\ 0)_{O3}} + d_{(1\ \bar{1}\ 0)_{O3}}\right] / 3$ in the O3 phase and to $\left[d_{(1\ 3\ \overline{1/3})_{O3'}} + d_{(\bar{1}\ 3\ 1/3)_{O3'}} + d_{(2\ 0\ \overline{2/3})_{O3'}}\right] / 3$ in the O3' phase. (**d**) Calculated ratio of *DoO* ($Li@TM_6$), *DoD* (LiO_2) and O vacancy plotted as a function of cycling time. (**e**) Schematic diagram of the $Li@TM_6$ superstructure in the O3' phase, in which Li and TM at the TMO_2 slabs occupy 2*b* and 4*g* Wyckoff sites, respectively.

Fig. 3 | LRM structure evolution viewed along the <100>$_{O3}$ projection. (**a-c**) In-plane orientation mapping of (**a**) a pristine particle, (**b**) a particle after a first charge to 4.5 V and (**c**) a particle after 100 cycles. The diffraction patterns were obtained from the purple and yellow areas in (**c**), which have mirror symmetry. The corresponding diffraction patterns of yellow and purple areas in (b) are familiar with those in (c). Note that in the pristine state, the particle is dominated by O3' phase, its orientation relationship with O3 is given in Supplementary Fig. 5.

Fig. 4 | LRM structure after cycling. (**a**) Atomic-resolution image of a representative region viewed along <100>$_{O3}$, showing changes to angles for the cathode charged to 4.5 V. (**b**) The unit-cell-by-unit-cell microstructural changes corresponding to the cyan area in (**a**), defined by the ratio *m/n*, where *m* and *n* are diagonal distance of the unit cell. (**c**) Magnified versions of areas I-IV in (**b**). (**d**) HAADF-STEM image showing an overview of a representative particle after 100 cycles. The interlayer and intralayer twinning boundaries are marked by green and orange arrows. (**e**) Atomic-resolution image of the area marked in (**d**), showing the interlayer

(001) coherent twinning boundary and intralayer {012} incoherent twinning boundaries. The inset shows an FFT of (e), which confirms the presence of a twinning-like structure (see Supplementary Fig.18). (**f**) High-resolution image of the area marked in (**e**), showing pore-like microstructures resulted from the intralayer twinning mediated frustration. The twinning variants are indicated by the white and pink frames.

Fig. 5 | Evolution process of nanoscale defects and TM migration. (**a**) Schematic diagram of phase evolution. (**b**) Schematic diagram of the correlation between defects and TM migration.

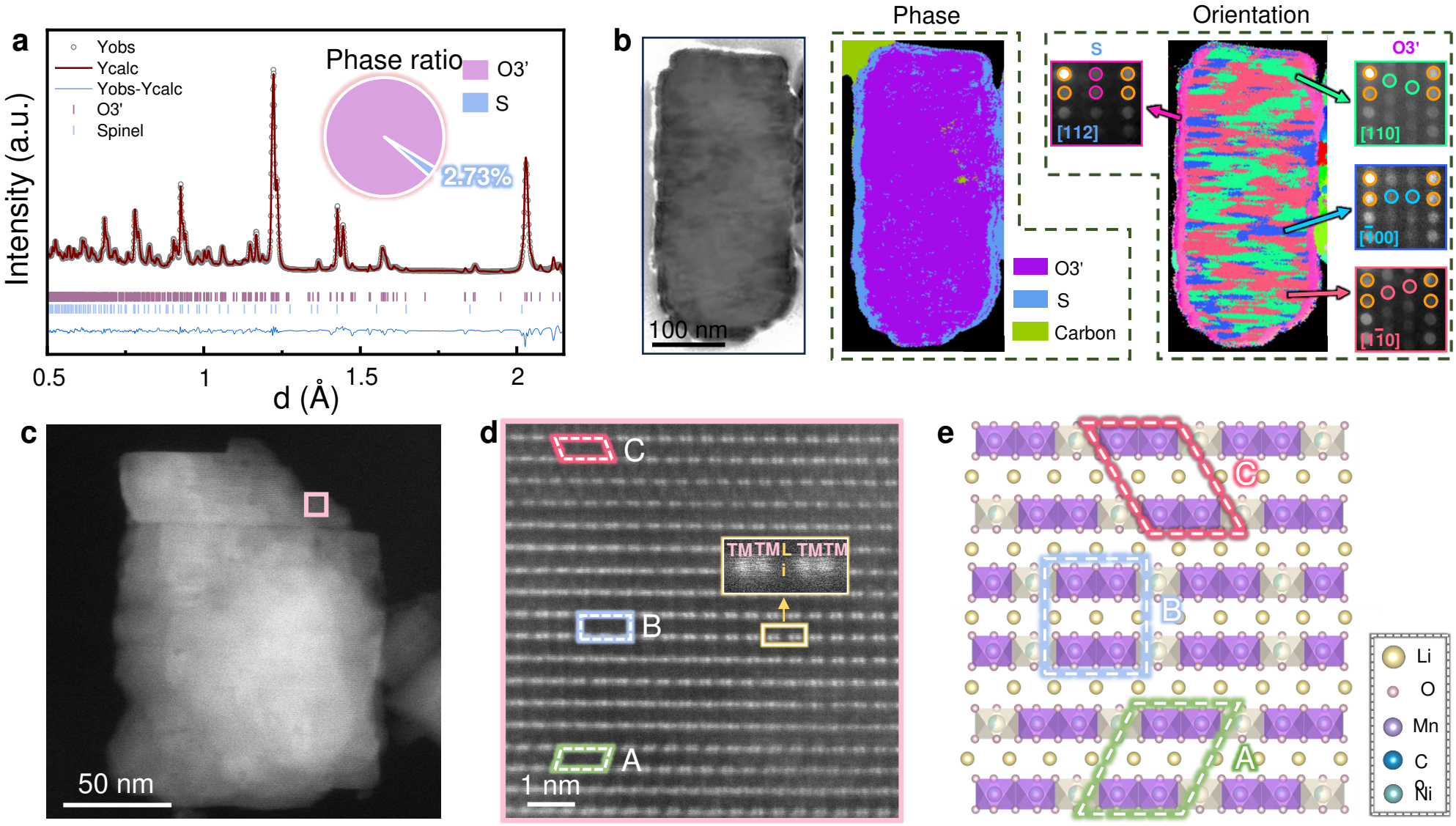
a
Yobs
Ycalc
Yobs-Ycalc
O3'
Spinel
Phase ratio
O3'
S
2.73%
Intensity (a.u.)
0.5
1
1.5
2
d (Å)
b
100 nm
Phase
Orientation
S
[112]
O3'
[110]
[$\bar{1}$00]
[1$\bar{1}$0]
O3'
S
Carbon
c
50 nm
d
C
TM TM L TM TM
i
B
A
1 nm
e
C
B
A
Li
O
Mn
C
Ni

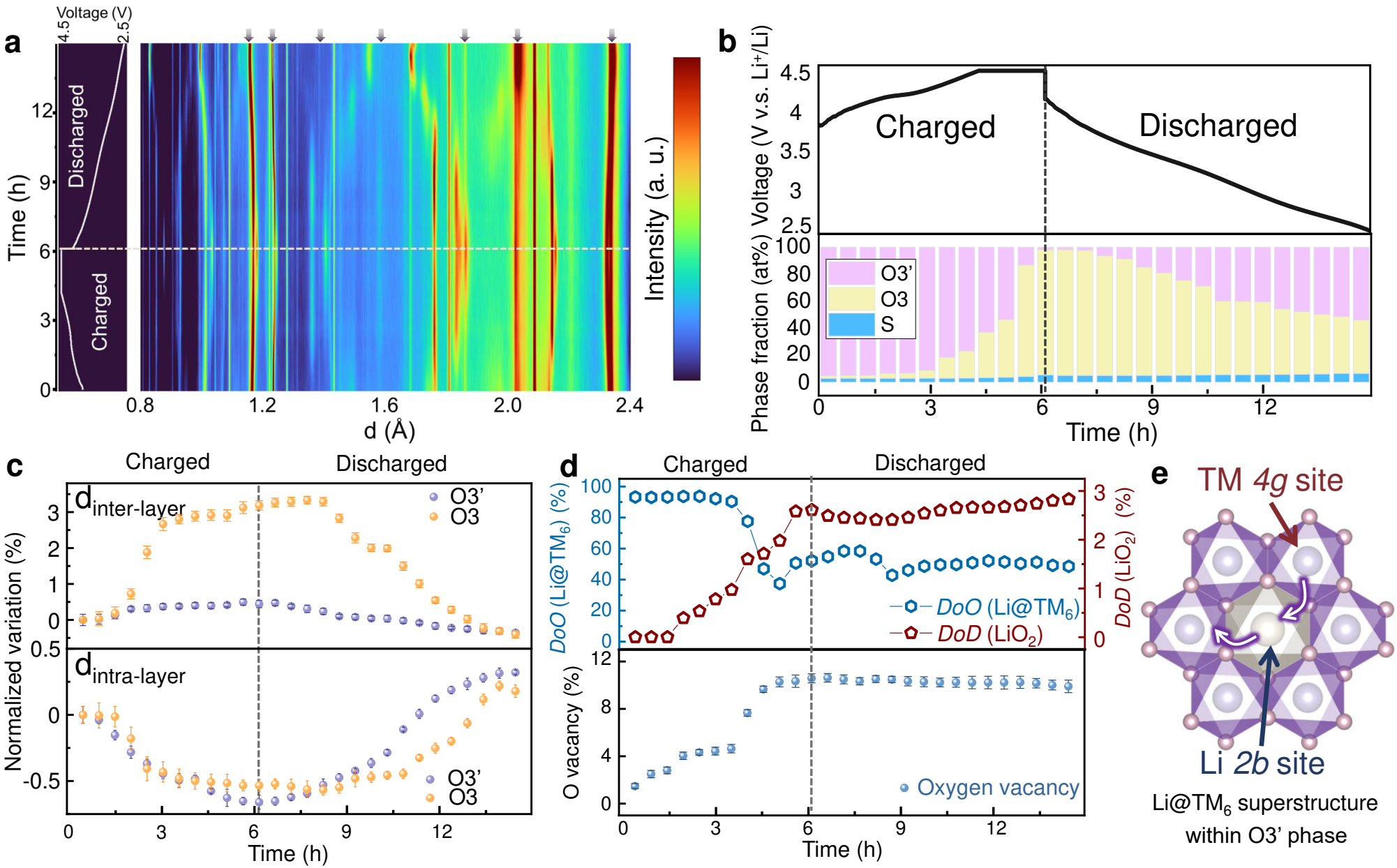
a
Voltage (V)
4.5
2.5
Discharged
Charged
Time (h)
d (Å)
Intensity (a. u.)
b
Charged
Discharged
Voltage (V v.s. Li+/Li)
Phase fraction (at%)
O3'
O3
S
Time (h)
c
Charged
Discharged
d inter-layer
d intra-layer
O3'
O3
Normalized variation (%)
Time (h)
d
Charged
Discharged
DoO (Li@TM6) (%)
DoD (LiO2) (%)
DoO (Li@TM6)
DoD (LiO2)
O vacancy (%)
Oxygen vacancy
Time (h)
e
TM 4g site
Li 2b site
Li@TM6 superstructure
within O3' phase

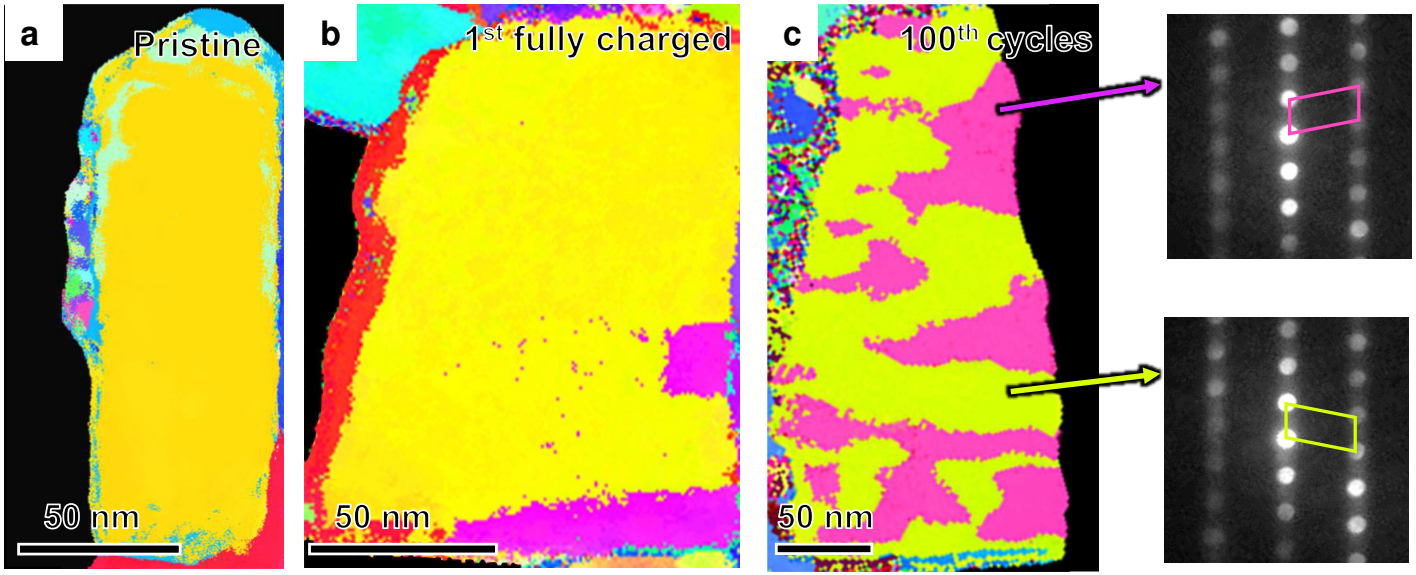
a
Pristine
50 nm
b
1st fully charged
50 nm
c
100th cycles
50 nm

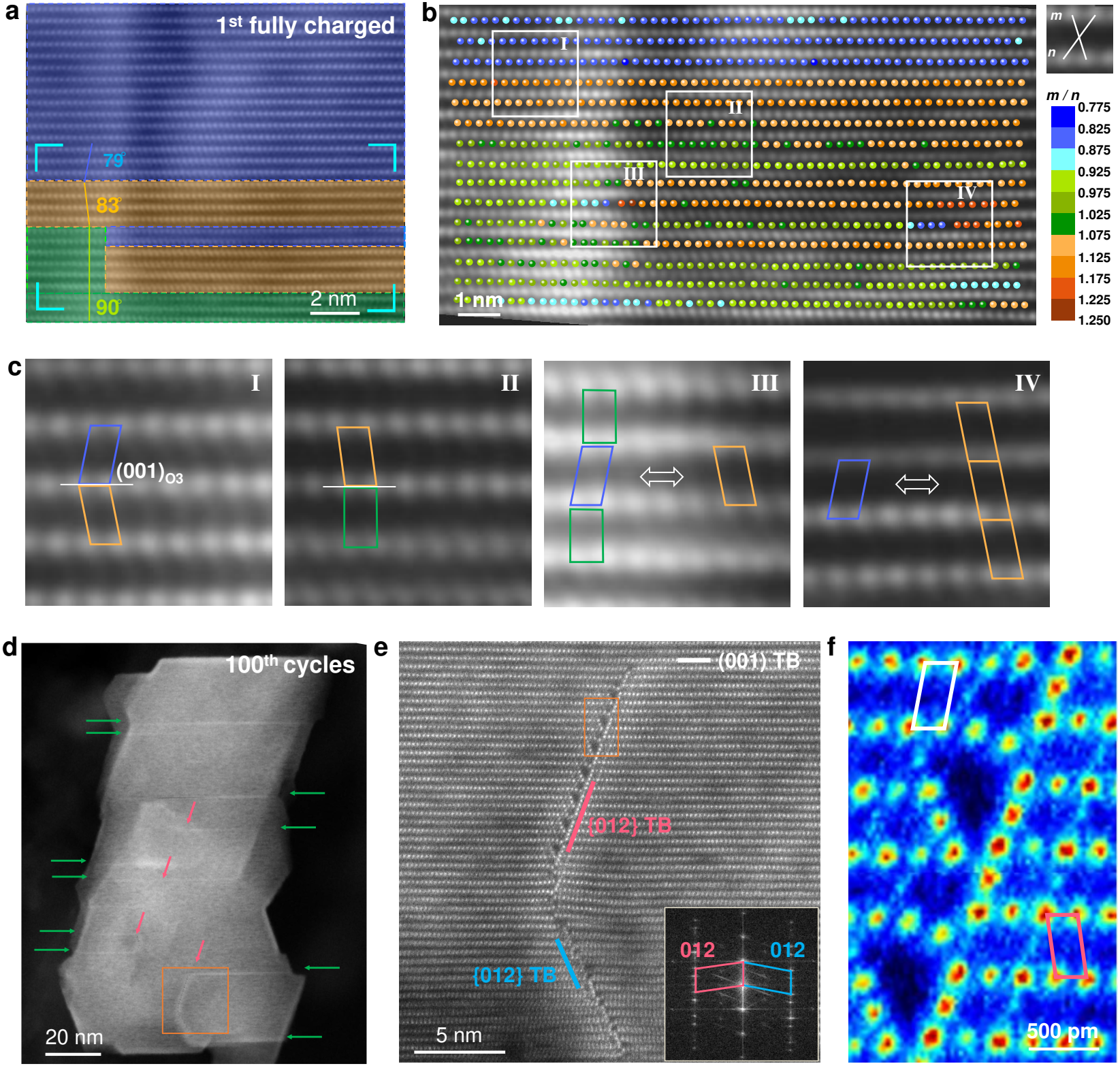
a
1st fully charged
79°
83°
90°
2 nm
b
I
II
III
IV
1 nm
m
n
m / n
0.775
0.825
0.875
0.925
0.975
1.025
1.075
1.125
1.175
1.225
1.250
c
I
II
III
IV
(001)O3
d
100th cycles
20 nm
e
(001) TB
{012} TB
{012} TB
012
012
5 nm
f
500 pm

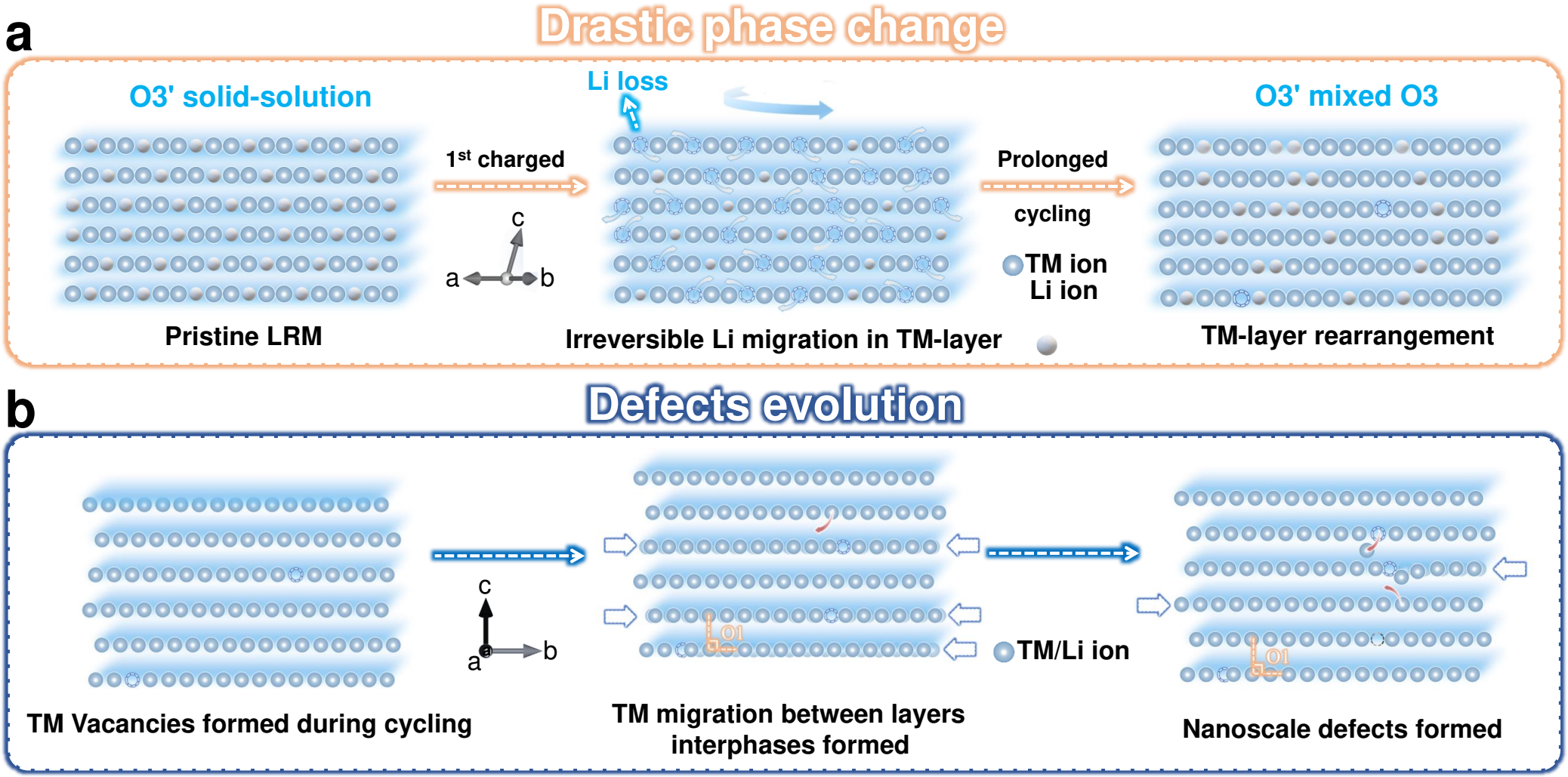
a
Drastic phase change
O3' solid-solution
Li loss
O3' mixed O3
1st charged
Prolonged
cycling
c
a
b
TM ion
Li ion
Pristine LRM
Irreversible Li migration in TM-layer
TM-layer rearrangement
b
Defects evolution
c
a
b
O1
TM/Li ion
TM Vacancies formed during cycling
TM migration between layers
interphases formed
Nanoscale defects formed

Supplementary Material for

Twinning mediated intralayer frustration governs structural degradation in layered Li-rich oxide cathode

Tingting Yang[1, 2, #], Maolin Yang[1, #], Zhongyuan Huang[1], Rui Wang[3], Tao Zeng[1], Peng-Han Lu[2], Wenhai Ji[4], Zenan Li[5], Jun Wang[5], Rafal E. Dunin-Borkowski[2], Lei Jin[2*], Yinguo Xiao[1*]

[1]School of Advanced Materials, Peking University, Shenzhen Graduate School, Shenzhen 518055, PR China

[2]Ernst Ruska-Centre for Microscopy and Spectroscopy with Electrons, Forschungszentrum Jülich GmbH, 52425 Jülich, Germany

[3]Department of Engineering, University of Cambridge, Cambridge CB30FS, UK

[4]Spallation Neutron Source Science Center, Dongguan 523803, PR China

[5]School of Innovation and Entrepreneurship, Southern University of Science and Technology, Shenzhen 518055, PR China

[#]These authors (T. Yang and M. Yang) contributed equally to this work.

[*]E-mail addresses: l.jin@fz-juelich.de (L. Jin); y.xiao@pku.edu.cn (Y. Xiao).

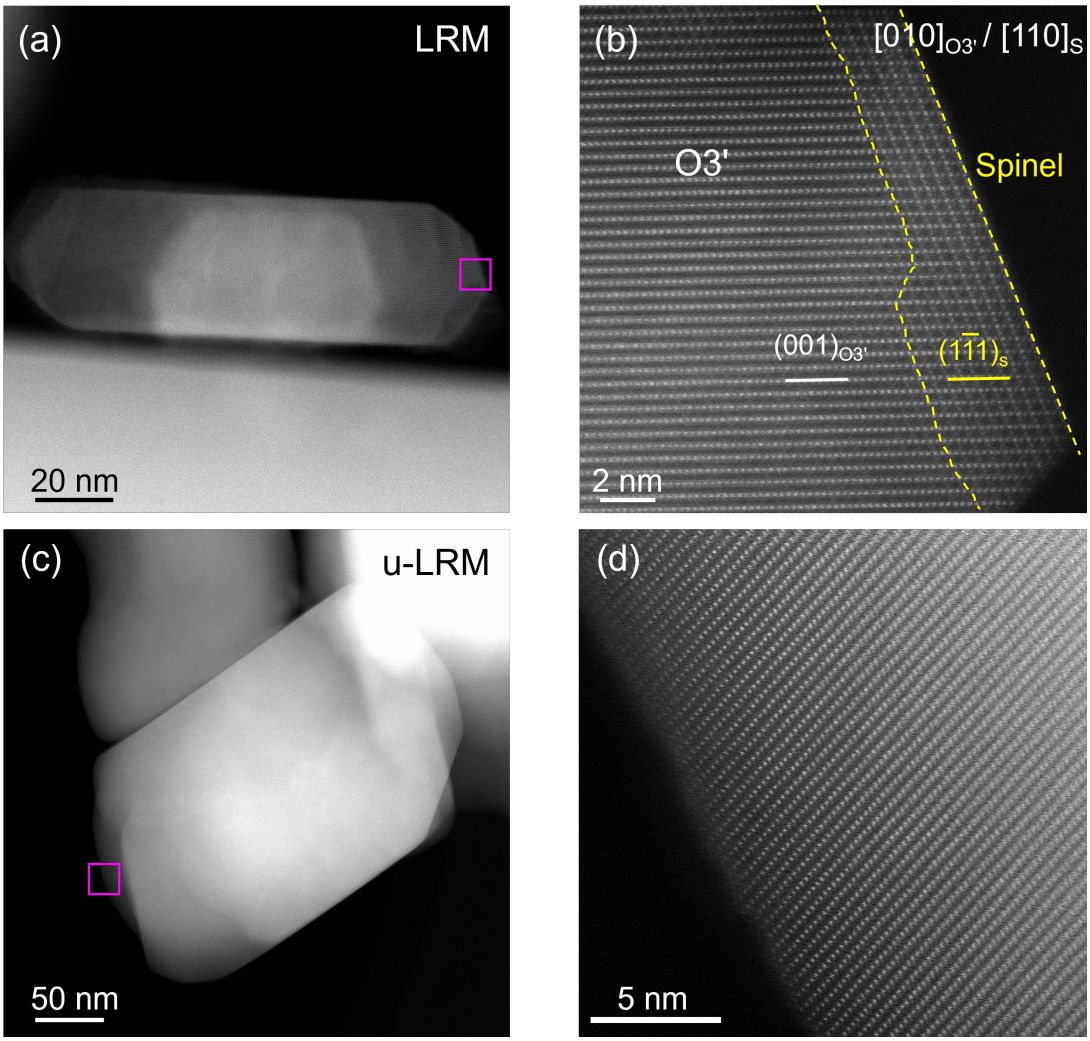

Supplementary Figure 1. (**a**) Low-magnification HAADF-STEM image of a pristine LRM nanoparticle. (**b**) Atomic-resolution HAADF-STEM image of the marked area in (**a**), showing a core/shell (O_3'/spinel) configuration. The orientation relationship between the spinel (S) shell and O_3' core is $[110]_S \parallel [010]_{O3'}$, $(1\bar{1}1)_S \parallel (001)_{O3'}$. (**c, d**) The morphology and the atomic-resolution HAADF-STEM image of the untreated LRM (u-LRM) nanoparticle.

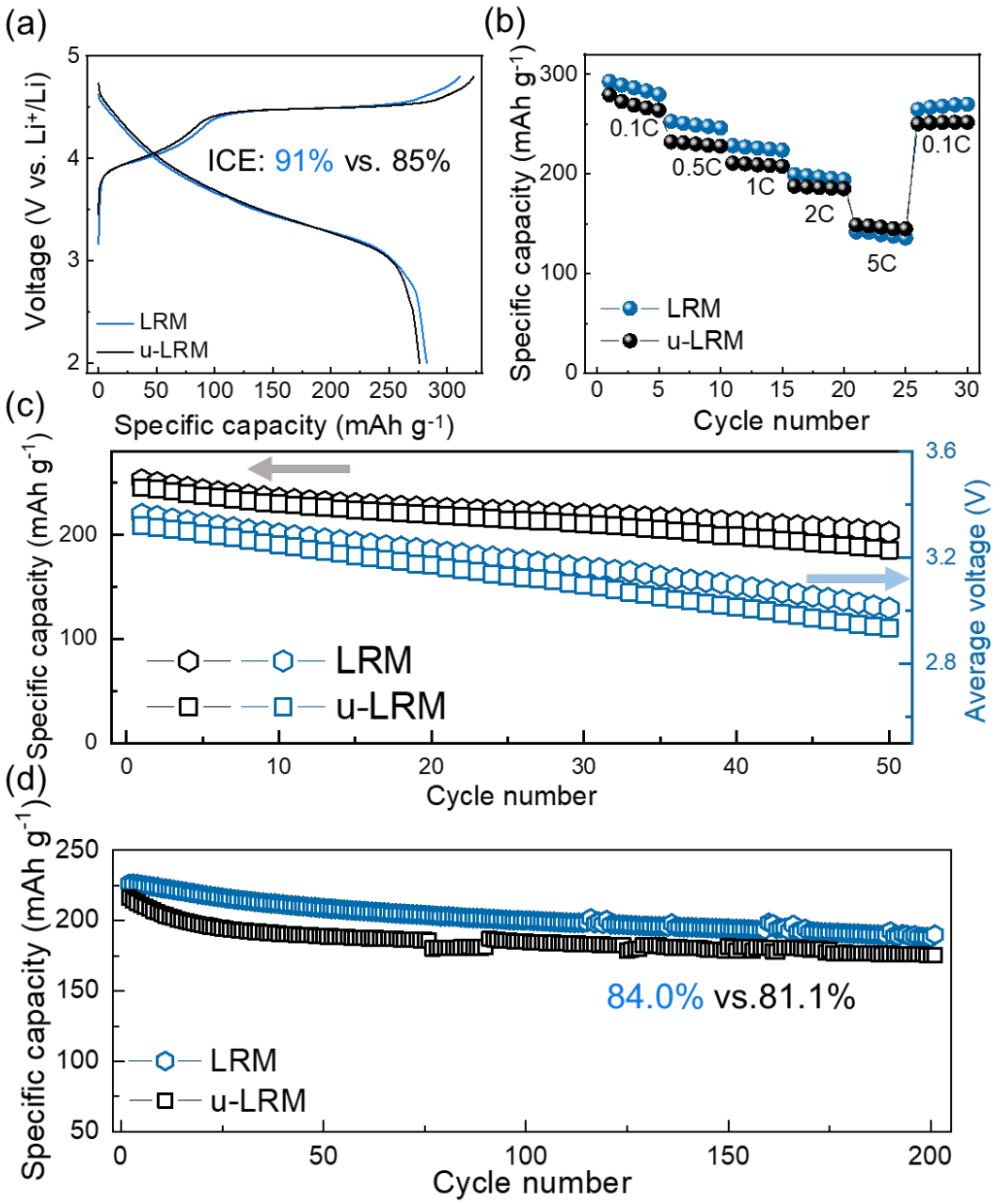

Supplementary Figure 2. Electrochemical LRM performance in a half cell. (a) Initial galvanostatic charge discharge (GCD) curve of the synthesized LRM and u-LRM during the first cycle within 2-4.8 V. (b) Rate performance of the synthesized LRM and u-LRM at various rates. (c) Long-term cycling retention and average voltage of the synthesized LRM and u-LRM at a rate of 0.5C (1C = 250 mA g^{-1}). (d) Long-term cycling retention of the synthesized LRM and u-LRM at a rate of 1C.

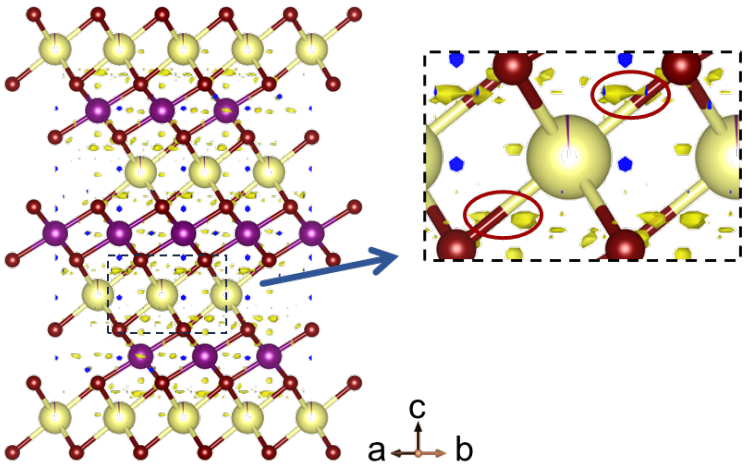

Supplementary Figure 3. Fourier difference map between observed data and O3' phase based on NPD result of LRM. Negative signal isosurface has been overlaid with a structural schematic of the O3 phase.

Rietveld refinement processes:

1. Calibration with Uncharged Neutron Diffraction:

A high-intensity neutron diffraction spectrum of the uncharged pouch cell was collected over an extended period of 60 minutes (compared to 30 minutes for each *operando* pattern). This allowed us to accurately determine the crystal structures of the electrochemically inactive Al and Cu current collectors. The structural parameters of these collectors were fixed, with only the 'scale' parameter adjusted to account for intensity variations due to differences in neutron beam flux.

2. Peak Shape Parameters:

Using the high-quality initial spectrum, peak shape factors for each compound involved in the *operando* processes were established and subsequently held constant during refinement.

3. Graphitic Anode Compounds:

The specific interplanar spacings of lithium-carbon compounds on the anode side (e.g., graphite, LiC_6, and LiC_{12}) remain unaffected by lithium intercalation or deintercalation. Therefore, lattice parameters for these phases were fixed based on the initial spectrum. Furthermore, the specific anode components could be clearly distinguished through diffraction peaks in the high d-value region.

4. Exclusion of Transition Metal Segregation in LRM Phases:

Based on STEM characterization results and to simplify the discussion, we did not consider elemental segregation of transition metals across the three LRM phases during refinement.

These adjustments led to a significantly improved goodness of fit across the full spectrum, thereby enhancing the reliability of the Rietveld refinement results and supporting a more accurate interpretation of the cathode's structural evolution.

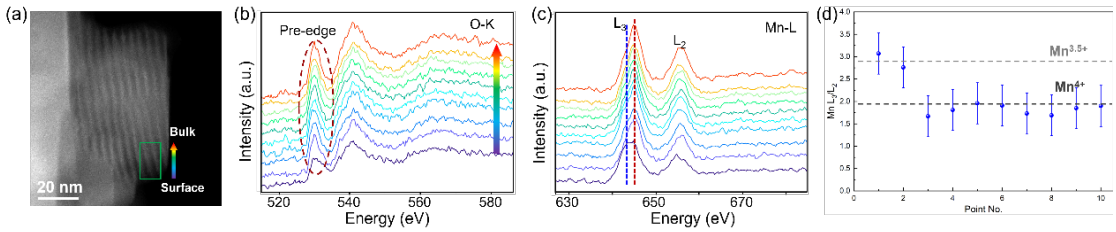

Supplementary Figure 4. (**a**) Annular dark-field STEM image of a pristine particle and (**b**, **c**) electron energy-loss spectra recorded at the (**b**) O-*K* and (**c**) Mn-$L_{2,3}$ edges from the marked area in (**a**). (**d**) Mn L_3/L_2 ratio calculated from (**c**). The dashed lines mark Mn valences of +3.5 and +4.0.[1]

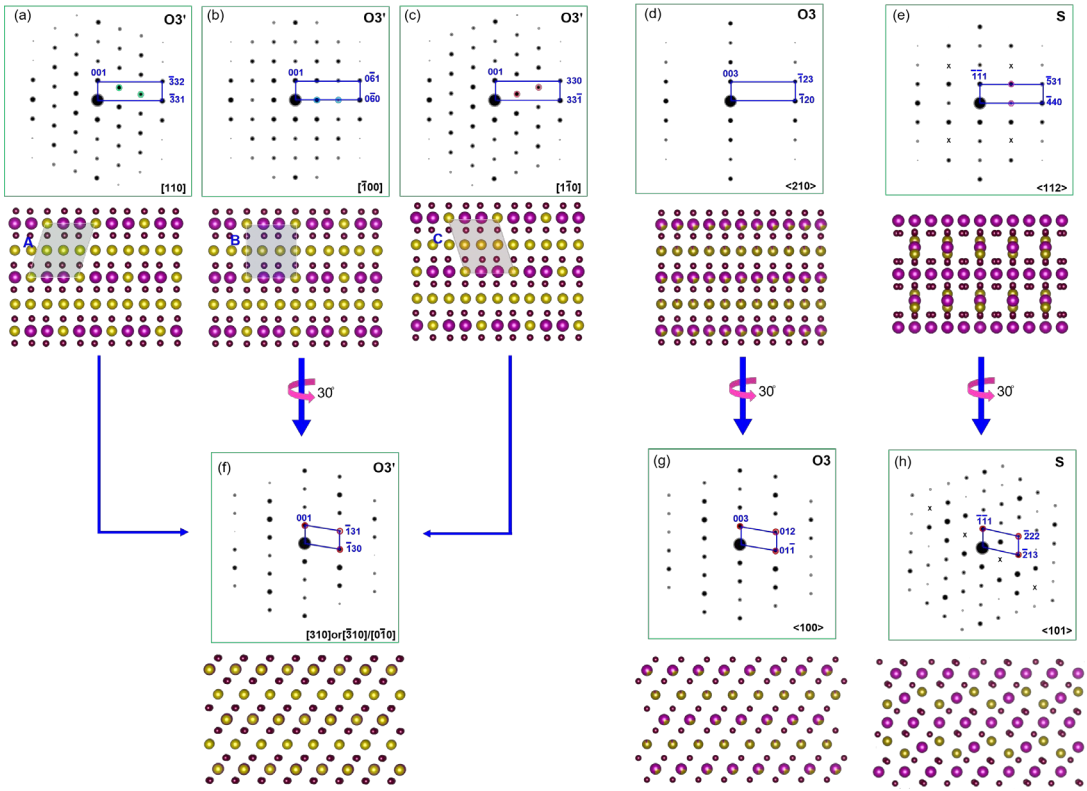

Supplementary Figure 5. Simulated diffraction patterns and corresponding atomic projections for O3', O3 and spinel (S), showing the orientation relationships among the three phases. (**a-c**) O3' [110], [$\bar{1}$00] and [1$\bar{1}$0] showing three configurations associated with TM-Li ordering. (**d**) O3 <210> projection showing TM-Li disordering. (**f**) O3 [310] (or [$\bar{3}$10]/ [0$\bar{1}$0]), along which all patterns are identical and TM-Li ordering becomes invisible. (**g**) O3 <100> showing the same patterns as (f). (**e**, **h**) Spinel <112> and <101> projections.

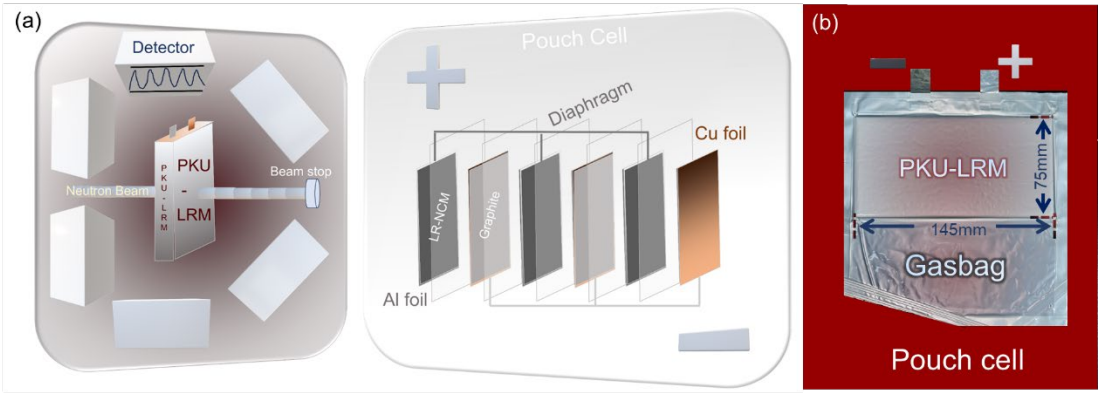

Supplementary Figure 6. (**a**) Schematic diagram of the *operando* neutron diffraction setup for the graphite || LRM pouch cell. (**b**) Photograph of an graphite || LRM pouch cell.

Graphite || LRM Pouch-cell	
Cathodes	**$Li_{1.2}Ni_{0.13}Co_{0.13}Mn_{0.54}O_2$**
Anode	**Graphite**
Pouch-cell Weight	**71.04 g**
Active Areas of Cathodes and Anodes (16 Poles of Each)	**145 × 75 mm^2 (Double-face)**
Cathode Mass Loading	**17.8 mg/cm^2**
Anode Mass Loading	**16.0 mg/cm^2**
N/P Radio	**1.1**
Electrolyte (1M LiF_6 TFTFE-FEMC-FEC)	**10 g**
Capacity of Cell (2.5 - 4.5 V)	**4 Ah**

Supplementary Figure 7. Design parameters of graphite || LRM pouch cell used in this work.

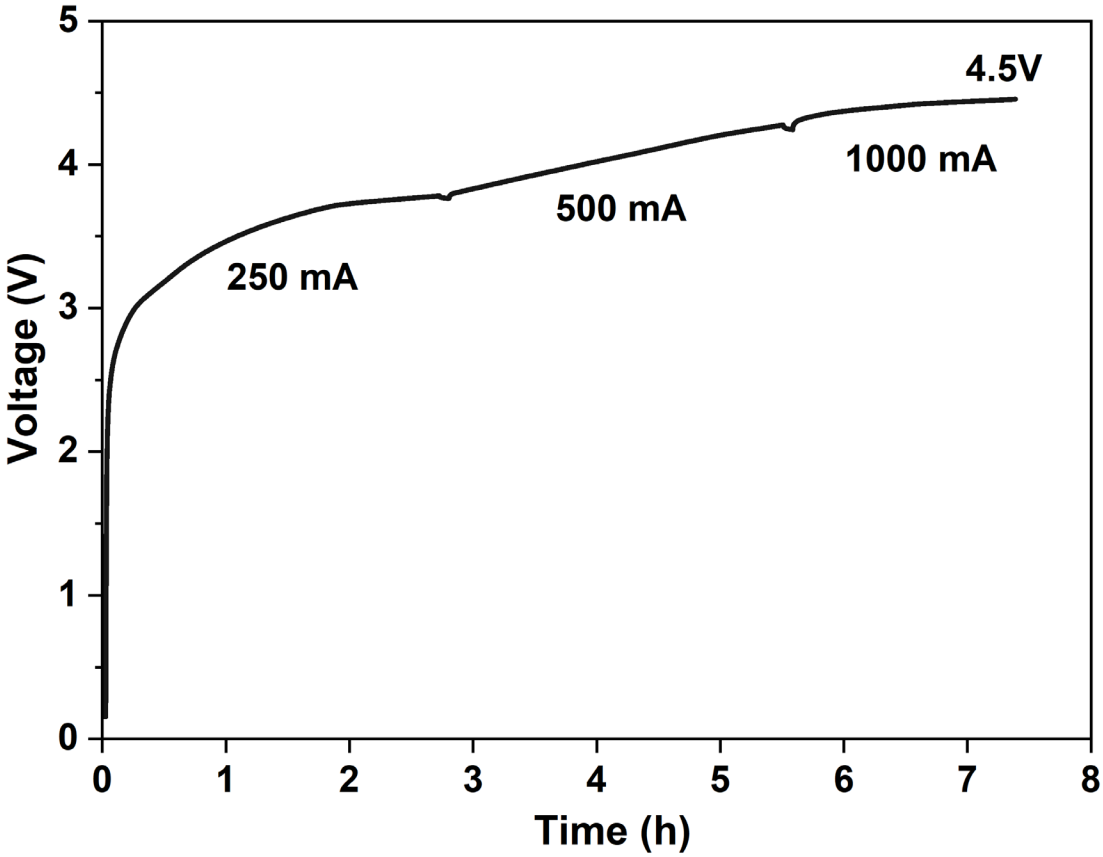

Supplementary Figure 8. The electrochemical curve of formation process in pouch cell.

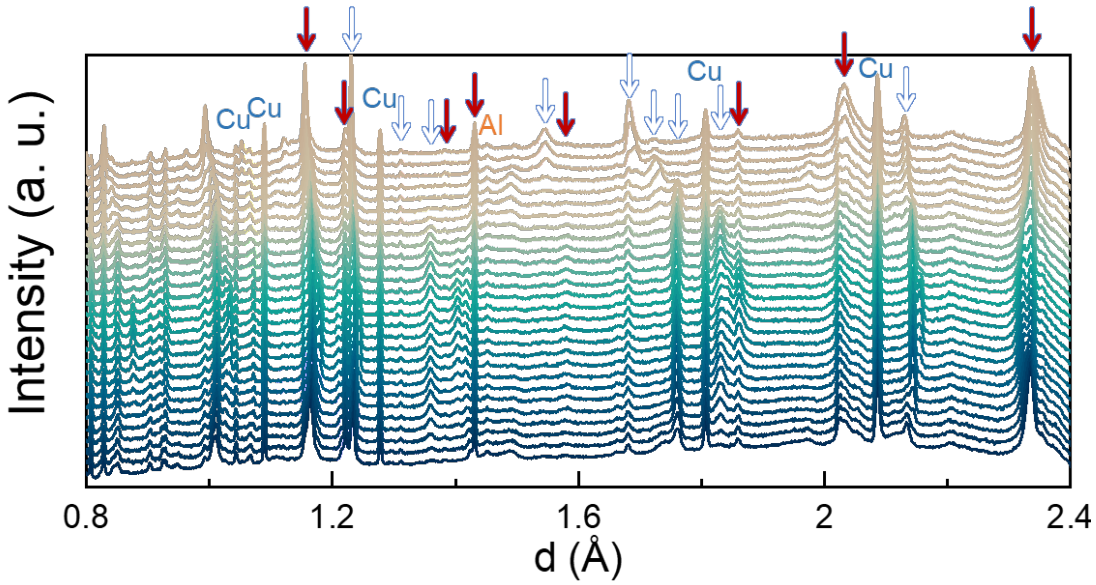

Supplementary Figure 9. The stacked plot of the operando neutron diffraction. The red arrow indexes the cathode, while the white arrow indexes the anode.

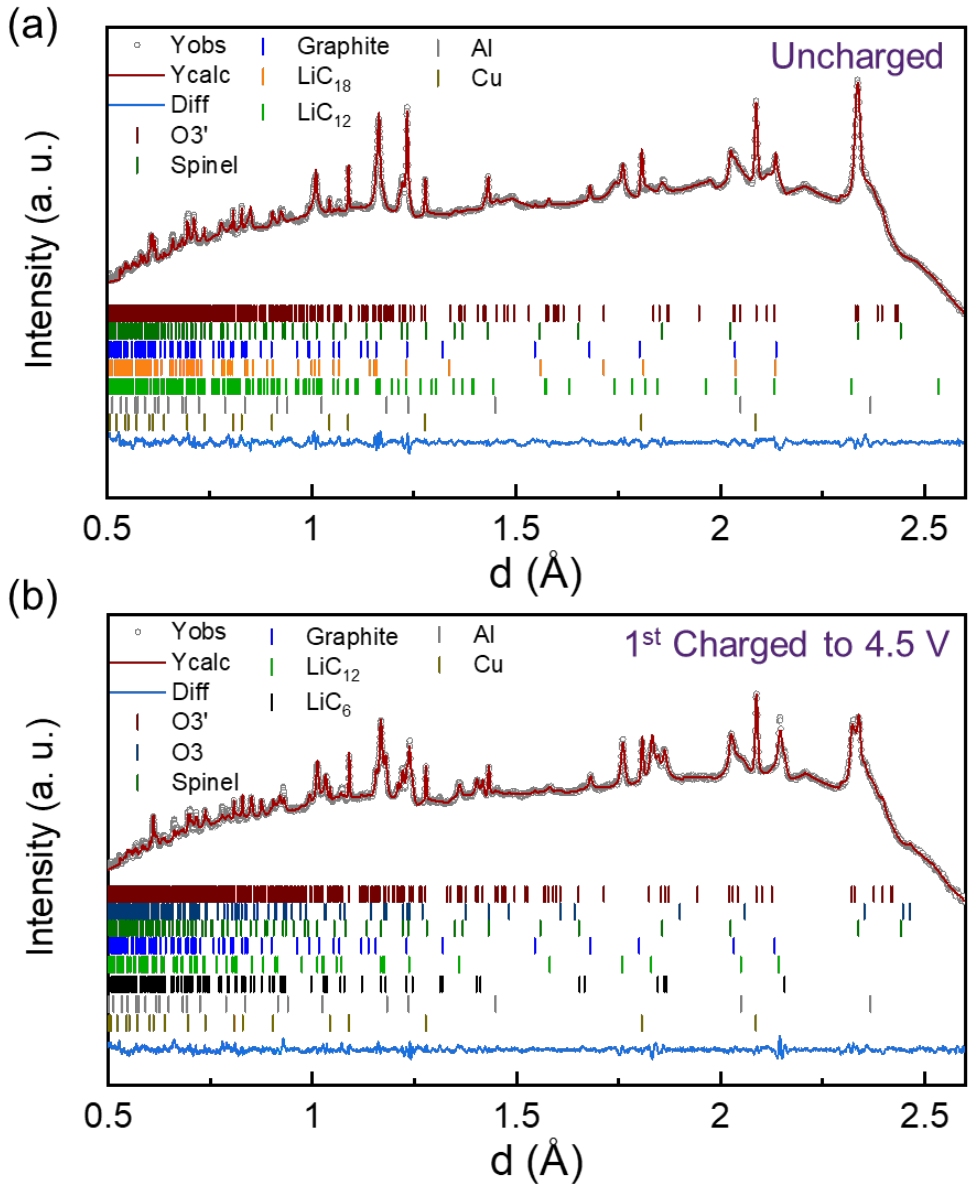

Supplementary Figure 10. (**a**, **b**) Refined neutron diffraction patterns recorded from the pouch cell (**a**) before and (**b**) after the first charge to 4.5 V. Bragg peak positions for the different phases, *i.e.*, different components in the pouch cell, are marked by short vertical bars in (**a**) and (**b**).

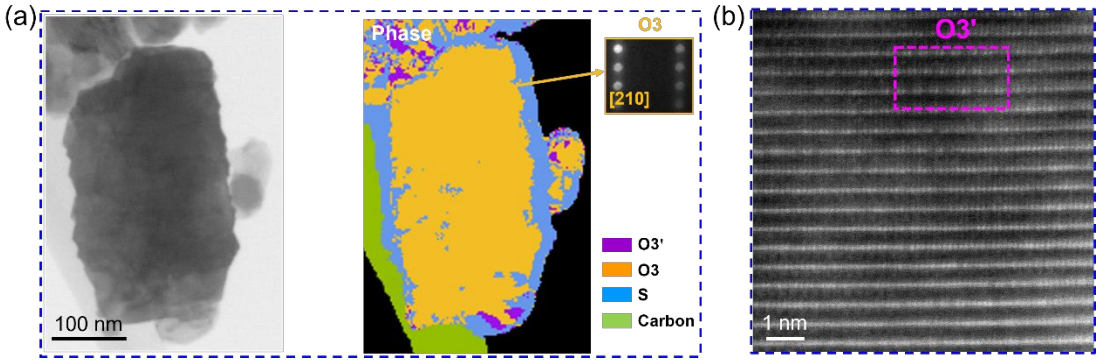

Supplementary Figure 11. Phase distribution in the cathode after first fully charged condition. (**a**) Phase mapping of the cathode after first fully charged along O3 [210] zone axis. (**b**) High-resolution HAADF-STEM image of the cathode after first fully charged, showing that only a small fraction of the O3' phase has remained, in agreement with the neutron diffraction results.

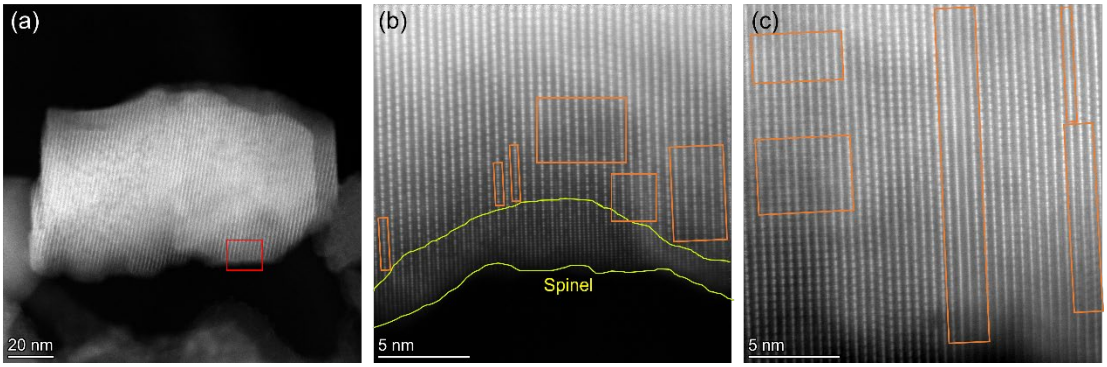

Supplementary Figure 12. (**a**) HAADF-STEM image showing an overview of a representative particle after first discharged to 2.5 V condition. (**b, c**) Atomic-resolution image of the area marked in (**a**), the O3 domains and the spinel phase are indicated by orange and yellow, respectively.

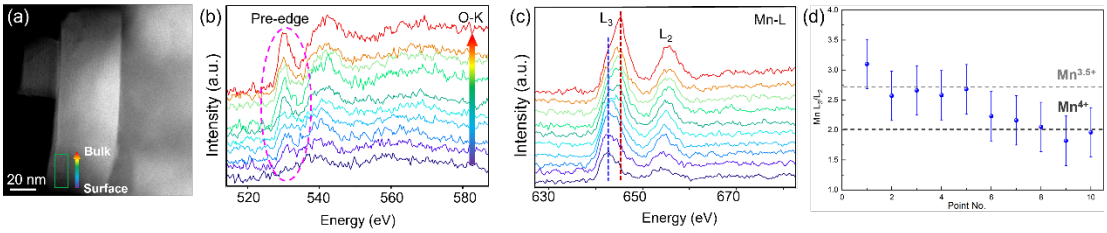

Supplementary Figure 13. (**a**) Annular dark-field STEM image and (**b**) O-*K* and (**c**) Mn-$L_{2,3}$ EELS fine structures recorded from the surface to the interior of a fully-charged LRM particle. (**d**) Mn L_3/L_2 ratio determined from (**c**), showing that the Mn valence does not change significantly after the first full charge.

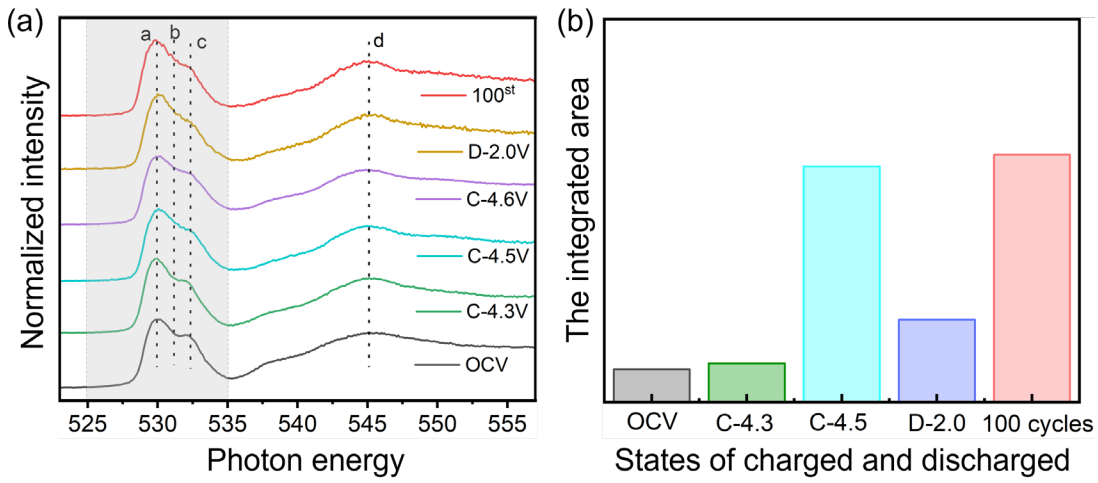

Supplementary Figure 14. (**a**) Normalized LRM O *K*-edge soft X-ray absorption spectra (sXAS) and (**b**) Integrated intensity between 525 and 535 eV for different charge/discharge states in the first cycle and after 100 cycles recorded in fluorescence yield mode.

Peaks a and c reflect O *2p*-Mn *3d* t_{2g} and O *2p*-Mn *3d* e_g orbital hybridization, respectively. Peak b emerged at high voltage (C-4.5 V), indicating O oxidation. The broadened peak d originates from the hybrid O *2p*-Mn *4sp* state. The integrated intensities from 525 to 535 eV reflect variations in O vacancies (holes). From OCV to C-4.3 V, the integrated intensities increase due to oxidation of TM atoms, which results in more empty orbitals. More O vacancies are generated on charging to 4.5 V. The integrated intensity decreases after discharging to 2.0 V, but remains higher than for OCV, implying O irreversibility during battery cycling. After 100 cycles (under OCV), the integrated intensity increases significantly, suggesting the formation of a large number of O vacancies and empty TM orbitals. This behavior is linked to the formation of a surface spinel structure.

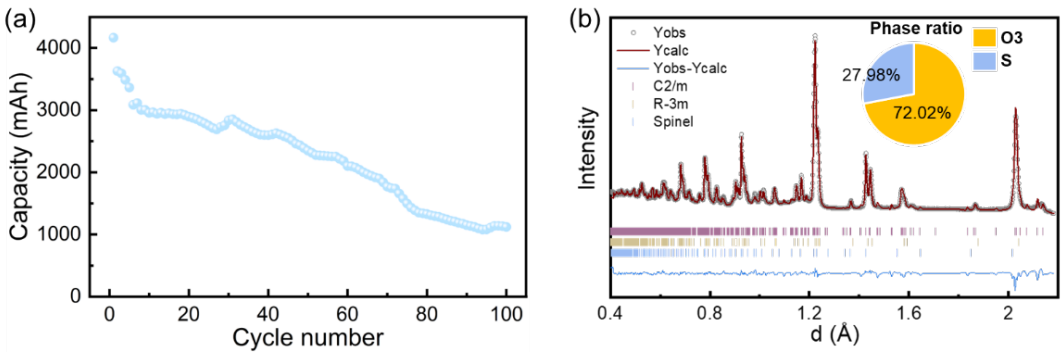

Supplementary Figure 15. (**a**) Long-term cycling retention of the pouch cell at a current of 4 A and at 2.0 – 4.5 V. (**b**) NPD and Rietveld refinement analysis of the LRM after 100 cycles. The inset sector plot shows the phase fraction distribution.

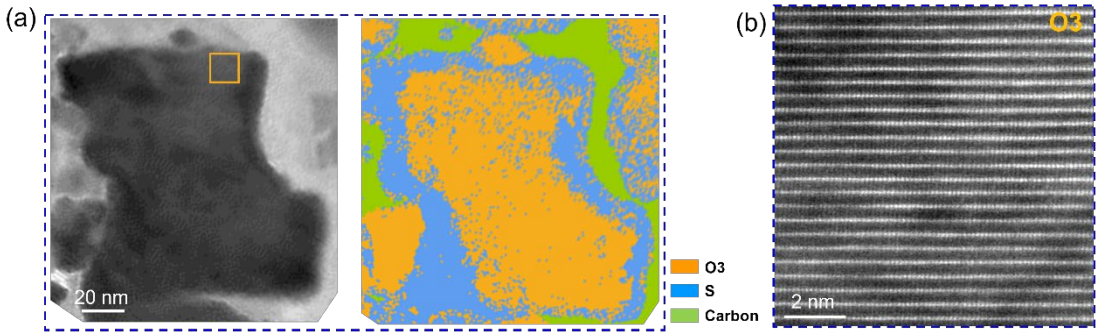

Supplementary Figure 16. (**a**) Phase mapping of the cathode after 100 cycles along O3 <210> zone axis. (**b**) High-resolution HAADF-STEM image showing that the atomic arrangement is disordered and no O3' phase is left after 100 cycles.

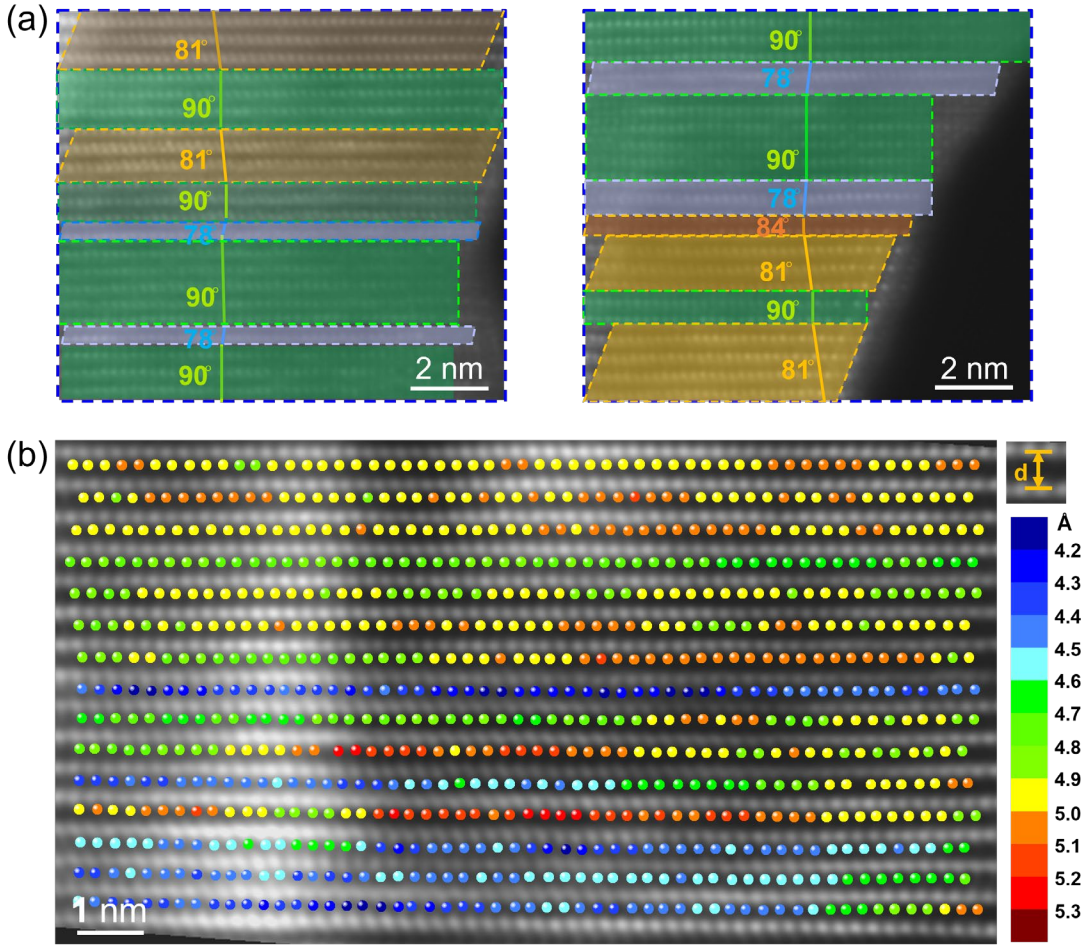

Supplementary Figure 17. (**a**) Atomic-resolution HAADF-STEM image of a cathode LRM particle charged to 4.5 V. (**b**) Simulated lattice value map of the area in Fig. 3d.

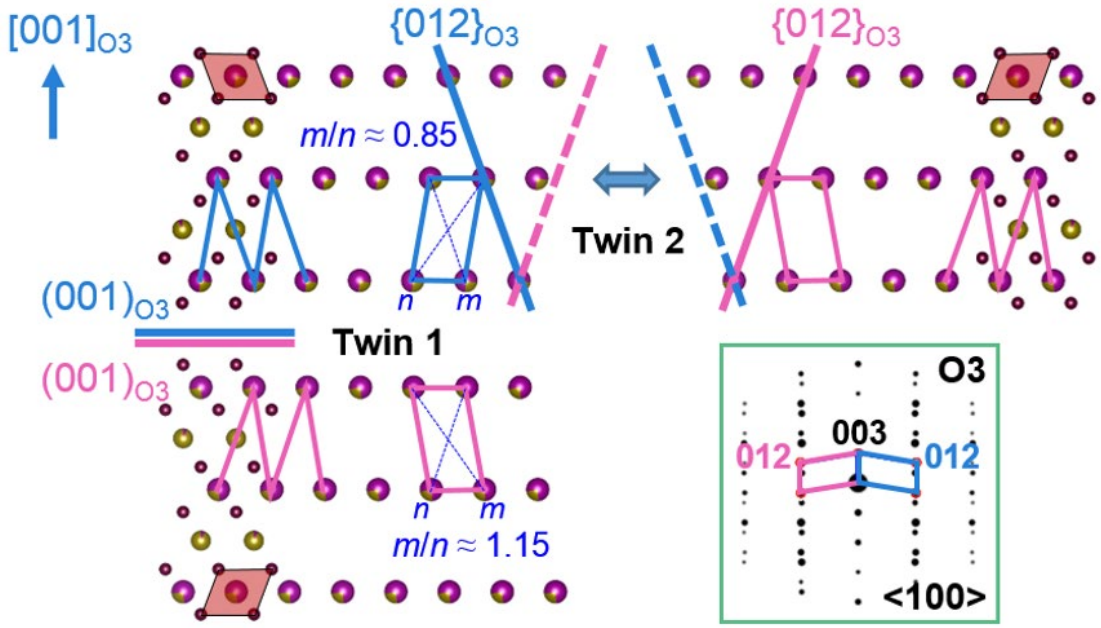

Supplementary Figure 18. Schematic illustration of two types of twinning configurations. Twin 1: $[001]_{O3}$ twin axis with twinning plane of $(001)_{O3}$, and Twin 2: $[001]_{O3}$ twin with twinning habit plane of $\{012\}_{O3}$. The simulated electron diffraction is calculated based on kinematical electron diffraction theory.

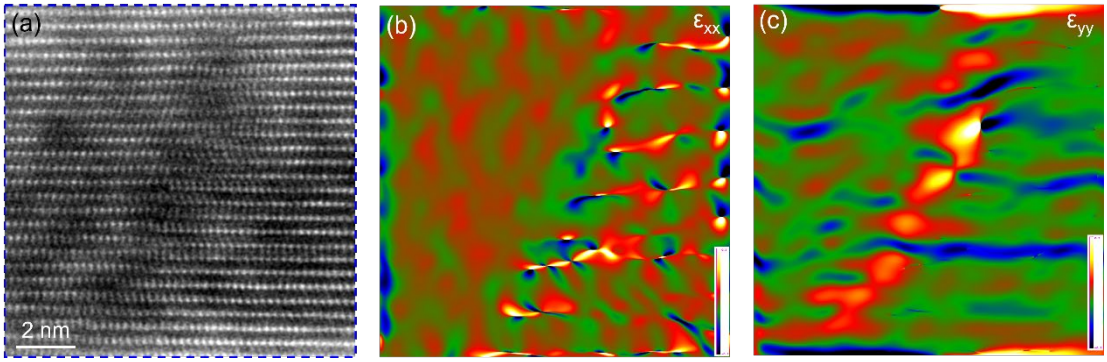

Supplementary Figure 19. (**b**) Horizontal ε_{xx} and (**c**) vertical ε_{yy} strain distributions obtained by applying geometrical phase analysis to the HAADF-STEM image shown in (**a**). The color scale spans strains of -20% (blue) to +20% (red).

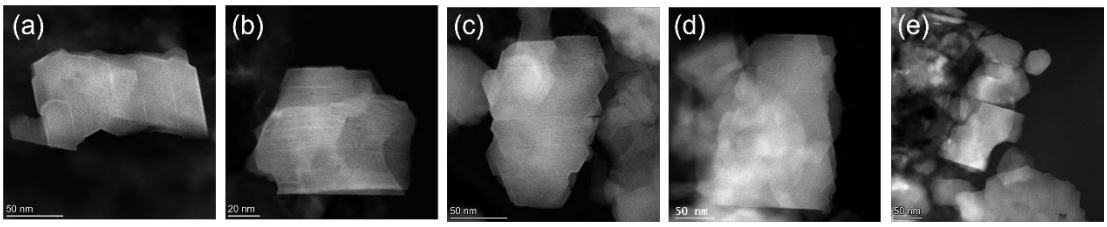

Supplementary Figure 20. Defects in the cathode material after 100 cycles.

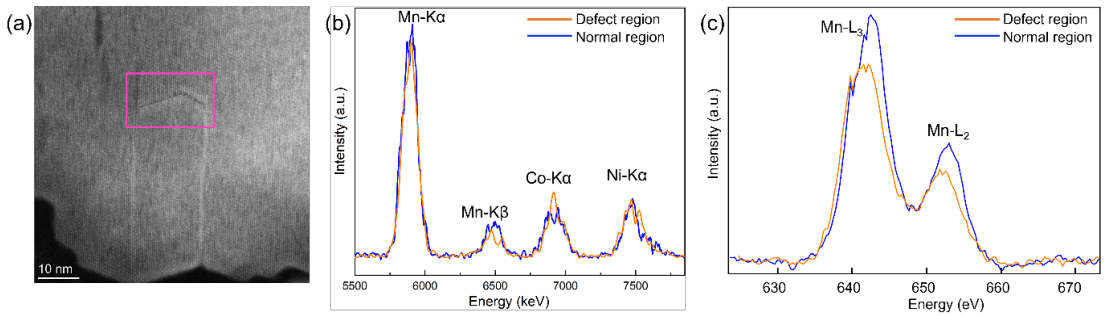

Supplementary Figure 21. (**a**) The overview HAADF-STEM image of LRM cathode after 100 cycles. (**b**) The EDS spectra showing the Mn, Co and Ni K edges from the specified region in (**a**). Decreased Mn concentration can be observed at the defect area. (**c**) The EELS spectra showing the Mn L edges of the selected area in (**a**), indicating the valence change of Mn in defect region.

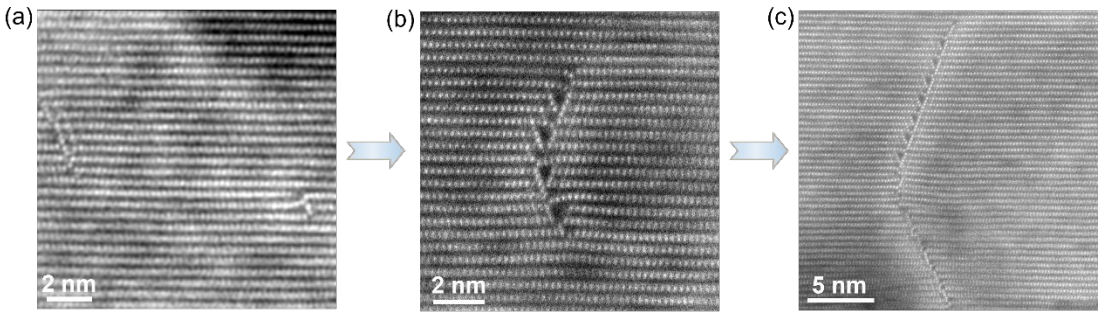

Supplementary Figure 22. Images showing the defect formation process.

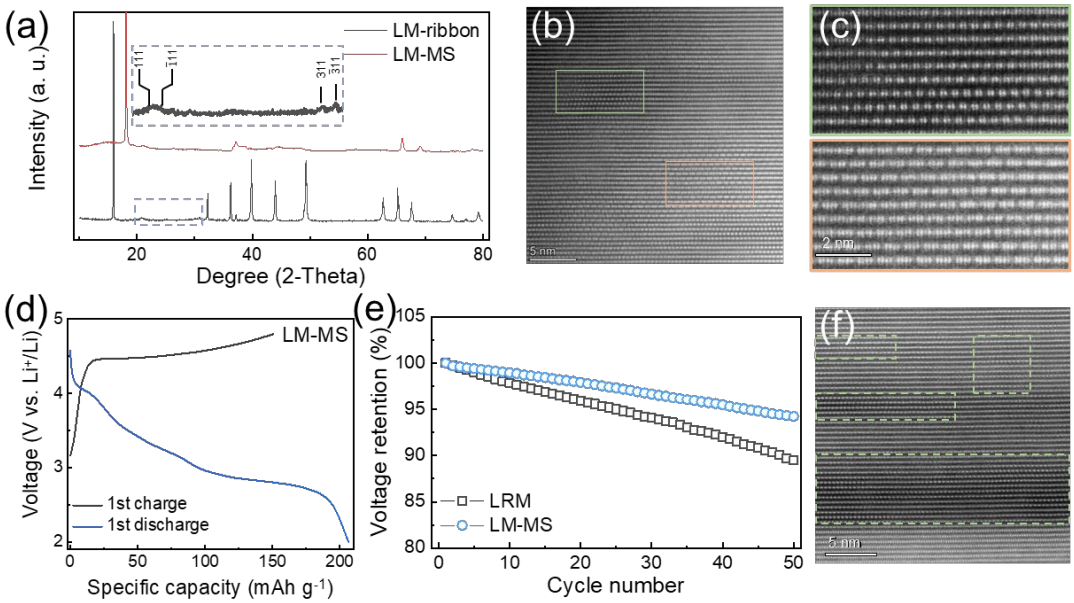

Supplementary Figure 23. (**a**) XRD patterns of $Na_{0.6}Li_{0.2}Mn_{0.8}O_2$ with a ribbon-type Li-Mn superlattice (denoted as LM-ribbon) and the ion-exchanged sample obtained via the molten salt method (denoted as LM-MS). (**b**) Low-magnification HAADF-STEM image of LM-MS. (**c**) High-resolution HAADF-STEM image of the marked region in (**b**), illustrating the atomic arrangement in the pristine LM-MS cathode, which features both honeycomb-type and ribbon-type structural domains. (**d**) Initial GCD curve of the synthesized LM-MS during the first cycle in the voltage range of 2–4.8 V. (**e**) Long-term average voltage retention of the synthesized LRM and LM-MS at a rate of 0.5C (1C = 250 mA g^{-1}). (**f**) HAADF-STEM image of LM-MS after 60 cycles at 0.5C.

Initially, a $Na_{0.6}Li_{0.2}Mn_{0.8}O_2$ cathode with a ribbon-type Li-Mn superlattice (denoted as LM-ribbon) was synthesized. Subsequently, a Li-rich oxide cathode with a partially preserved ribbon-type Li-Mn superlattice (denoted as LM-MS) was obtained via a molten salt substitution method, as shown in Supplementary Fig. 22b, c. This ribbon-type structure alleviated the intralayer rearrangement of transition metals, significantly reducing voltage hysteresis (Supplementary Fig. 22d). Furthermore, it mitigated interlayer migration of transition metals to some extent, effectively delaying voltage decay (Supplementary Fig. 22e).

Remarkably, after 60 cycles at 0.5C, the LM-MS cathode retained its transition metal layer superlattice without developing pore-like microstructures illustrated in Fig. 4e, f (Supplementary Fig. 19f). This indicates a substantial improvement in structural stability.

Supplementary Table 1. Proportions of O3' and spinel phase in the pristine cathode powder and crystal cell parameters.

O3' (*C2/m*): 97.27 at%						
Atom	***Wyckoff***	***x***	***y***	***z***	B_{iso} (Å^2)	***Occ.***
O	8*j*	0.251(3)	0.323(3)	0.224(1)	0.437(1)	0.997(2)
O	4*i*	0.219(1)	0	0.224(1)	0.437(1)	1
Mn	4*g*	0	0.169(2)	0	1.692(1)	0.783(2)
Li	4*g*	0	0.169(2)	0	1.692(1)	0.021(2)
Co	4*g*	0	0.169(2)	0	1.692(1)	0.194(1)
Ni	4*g*	0	0.169(2)	0	1.692(1)	0.001(1)
Li	2*b*	0	1/2	0	4.439(6)	0.561(5)
Ni	2*b*	0	1/2	0	4.439(6)	0.385(5)
Mn	2*b*	0	1/2	0	4.439(6)	0.053(1)
Co	2*b*	0	1/2	0	4.439(6)	0.001(1)
Li	4*h*	0	0.662(2)	1/2	1.011(2)	0.998(5)
Ni	4*h*	0	0.662(2)	1/2	1.011(2)	0.001(1)
Mn	4*h*	0	0.662(2)	1/2	1.011(2)	0.001(1)
Li	2*c*	0	0	1/2	1.389(4)	0.998(5)
Ni	2*c*	0	0	1/2	1.389(4)	0.001(1)
Mn	2*c*	0	0	1/2	1.389(4)	0.001(1)
a = 4.940(1) Å, b = 8.550(1) Å, c = 5.028(1) Å, $\alpha = \gamma$ =90°, β = 109.333(1)°.						
Spinel: 2.73 at%						
Atom	***Wyckoff***	***x***	***y***	***z***	B_{iso} (Å^2)	***Occ.***
O	32*e*	0.250(2)	0.250(2)	0.250(2)	1.871(7)	1
Mn	16*d*	1/2	1/2	1/2	0.569(8)	2/3
Co	16*d*	1/2	1/2	1/2	0.569(8)	1/6
Ni	16*d*	1/2	1/2	1/2	0.569(8)	1/6
Li	8*a*	1/8	1/8	1/8	0.868(5)	1
$a = b = c$ = 8.067(7) Å, $\alpha = \beta = \gamma$ = 90°.						
R_p: 2.19%, R_{wp}: 2.53%, R_{exp}: 0.14%.						

Supplementary Table 2. Proportions of O3' and spinel phase in the uncharged cathode and crystal cell parameters.

O3' (*C2/m*): 97.16 at%						
Atom	***Wyckoff***	***x***	***y***	***z***	***B_{iso} (Å^2)***	***Occ.***
O	8*j*	0.256(2)	0.324(5)	0.223(7)	0.252(1)	0.995(1)
O	4*i*	0.216(2)	0	0.223(7)	0.252(1)	1
Mn	4*g*	0	0.167(1)	0	2.059(2)	0.784(2)
Li	4*g*	0	0.167(1)	0	2.059(2)	0.021(2)
Co	4*g*	0	0.167(1)	0	2.059(2)	0.194(1)
Ni	4*g*	0	0.167(1)	0	2.059(2)	0.001(1)
Li	2*b*	0	1/2	0	5.667(6)	0.561(2)
Ni	2*b*	0	1/2	0	5.667(6)	0.385(2)
Mn	2*b*	0	1/2	0	5.667(6)	0.053(2)
Co	2*b*	0	1/2	0	5.667(6)	0.001(1)
Li	4*h*	0	0.662(3)	1/2	0.786(5)	0.956(4)
Ni	4*h*	0	0.662(3)	1/2	0.786(5)	0.001(1)
Mn	4*h*	0	0.662(3)	1/2	0.786(5)	0.001(1)
Li	2*c*	0	0	1/2	0.956(4)	0.956(4)
Ni	2*c*	0	0	1/2	0.956(4))	0.001(1)
Mn	2*c*	0	0	1/2	0.956(4)	0.001(1)
a = 4.947(3) Å, b = 8.544(1) Å, c = 5.029(8) Å, $\alpha = \gamma$ =90°, β = 109.25(3)°.						
Spinel: 2.84 at%						
Atom	***Wyckoff***	***x***	***y***	***z***	***B_{iso} (Å^2)***	***Occ.***
O	32*e*	0.246(3)	0.246(3)	0.246(3)	0.831(2)	1
Mn	16*d*	1/2	1/2	1/2	1.121(3)	2/3
Co	16*d*	1/2	1/2	1/2	1.121(3)	1/6
Ni	16*d*	1/2	1/2	1/2	1.121(3)	1/6
Li	8*a*	1/8	1/8	1/8	0.175(1)	1
$a = b = c$ = 8.091(2) Å, $\alpha = \beta = \gamma$ = 90°.						
R_p: 0.884%, R_{wp}: 1.09%, R_{exp}: 0.36%.						

Supplementary Table 3. Proportions and structural information about O3 and spinel phases in the LRM cathode after 100 cycles.

O3 (*R-3m*): 72.02 at%						
Atom	***Wyckoff***	***x***	***y***	***z***	B_{iso} **(Å²)**	***Occ.***
O	6*c*	0	0	0.736(5)	1.467(3)	0.997(9)
Li	3*a*	0	0	0	3.603(7)	0.431(3)
Ni	3*a*	0	0	0	3.603(7)	0.002(3)
Ni	3*b*	0	0	1/2	3.603(7)	0.127(3)
Li	3*b*	0	0	1/2	3.600(9)	0.082(3)
Mn	3*b*	0	0	1/2	3.600(9)	0.539(1)
Co	3*b*	0	0	1/2	3.600(9)	0.130(1)
$a = b = 2.840(8)$ Å, $c = 14.539(2)$ Å, $\alpha = \beta = 90°$, $\gamma = 120°$.						
Spinel: 27.98 at%						
Atom	***Wyckoff***	***x***	***y***	***z***	B_{iso} **(Å²)**	***Occ.***
O	32*e*	0.233(8)	0.233(8)	0.233(8)	0.213(1)	0.978(6)
Mn	16*d*	1/2	1/2	1/2	0.220(2)	2/3
Co	16*d*	1/2	1/2	1/2	0.220(2)	1/6
Ni	16*d*	1/2	1/2	1/2	0.220(2)	1/6
Li	8*a*	1/8	1/8	1/8	0.579(2)	0.728(2)
$a = b = c = 8.173(5)$ Å, $\alpha = \beta = \gamma = 90°$.						
R_p: 1.32%, R_{wp}: 1.47%, R_{exp}: 0.27%.						

Supplementary Table 4. Measured defect densities of the samples after 100 cycles.

	Particle 1	**Particle 2**	**Particle 3**	**Particle 4**	**Particle 5**
Number of defects	6	5	4	4	6

Supplementary References

1 Tan, H., Verbeeck, J., Abakumov, A., can Tendeloo, G. Oxidation state and chemical shift investigation in transition metal oxides by EELS. *Ultramicroscopy* **116**, 24-33 (2012).